mathematics

Article

Video Distance Measurement Technique Using Least Squares Based Sharpness Cost Function

Elena Serea [1,*], Mihai Penciuc [2], Marinel Costel Temneanu [1] and Codrin Donciu [1]

[1] Faculty of Electrical Engineering, "Gheorghe Asachi" Technical University of Iași, 700050 Iași, Romania
[2] Faculty of Industrial Design and Business Management, "Gheorghe Asachi" Technical University of Iași, 700050 Iași, Romania
* Correspondence: edanila@tuiasi.ro; Tel.: +40-0040740481758

Abstract: A wide range of precision applications requires video measuring systems that achieve a large number of successive measurements and deliver fast results. Their efficiency is essentially given by the technical performances of the used equipment and by the measurement technique on which they operate. In order to enhance the reliability of such a system, the paper presents a new method of measuring the distance with a single video camera intended to assess the distance at which the object of interest to the camera is located. The technique makes use of a least squares-based sharpness cost function and determines the distance between the camera and the object of interest by minimizing the least squares deviation of the current sharpness values from the sharpness values obtained by calibration. It involves the current sharpness calculation phase, the normalization phase, the phase of calculating the deviations of the current sharpness from the dependencies obtained by calibration and the phase of determining the minimum deviation index.

Keywords: image; distance measurement; lens; sharpness; least squares method; polynomial

MSC: 65D19

check for updates

Citation: Serea, E.; Penciuc, M.; Temneanu, M.C.; Donciu, C. Video Distance Measurement Technique Using Least Squares Based Sharpness Cost Function. *Mathematics* **2022**, *10*, 3273. https://doi.org/10.3390/math10183273

Academic Editor: Junlin Hu

Received: 26 July 2022
Accepted: 7 September 2022
Published: 9 September 2022

1. Introduction

Optical distance determination can be performed by active and passive methods [1]. Active emitter-receiver methods are based on computing the time of flight for a light, ultrasound or radio beam emitted to the object of interest, which after reflection, is received by the video camera [2]. The beam contains a known pattern, and the method of determining the distance is based on measuring the deformation of the pattern [3,4]. There were several products developed that were subjected to this active method, each with its complexity and hardware limits: ARCore, a Google platform for building augmented reality [5], Occipital's Structure Sensor for 3D scanning [6], Kinovea analysis software for sport and medical professionals [7] or Microsoft's Kinect, a motion controller for gaming peripherals [8]. Research and advances in optical systems [9–11] regarding optical transmitter-receiver application in video communication are also acquainted [12–14] but preserve the potential confusion of echoes from previous or subsequent beam pulses or from other systems. Moreover, these applications require expensive and specialized equipment to operate, depending on calibration accuracy [15,16] and a limit of 4 m distance to be measured [17].

Passive methods for distance measuring are based on cameras and computer vision techniques, generally using two-chamber binocular systems between which the distance is accurately known [18]. These methods are based on information about the object's position, thus requiring a precise alignment of the two cameras' captured images to identify the correspondence between the object of interest's images [19–21]. The issue of disparity between corresponding pixels in the two images was removed through the adoption of deep convolutional neural networks, whose gain depends on the images' resolution and on the number of iterations the application requires [22,23]. Another approach for image stitching is a feature-based technique, which extracts point-by-point characteristics from two or more images using different algorithms to compose a panoramic image. They compare all pixels' intensities with each other or determine a correspondence between images through distinct features extracted from the processing [24,25]. One popular IT device built on this principle is Dell Venue 8 7000 Series, whose stereoscopic cameras allow measuring length, width, and height and calculating particular areas through photos. A derived variant of the binocular method uses a single camera moving over a known distance, obtaining the binocular effect. This concept finds most of its applications in the optical 3D shape reconstruction field [26–28] or for obstacle avoidance [29], with the downside of a large amount of data that have to be captured and processed. The precision and test–retest reliability of image reconstruction have been improved by distance measurement methods based on the correspondence between the position of the focus lens and the distance the object is from the camera, known as shape from focus or depth from focus [30–32]. To accurately generate a map of the scene, the distance from the camera must be calculated for every point by measuring its relative degree of focus in the images where the point appears [33], so the performance of using the focus in determining the distance depends on the number of positions that the focus lens can have. In shape from focus applications, the process of Gaussian interpolation for creating new data points using a given discrete set of data has the widest practice. Gaussian interpolation uses three focus values (the maximum and two adjacent values) and has been proposed since 1994 [34]. To some extent, linear and quadratic interpolation are adopted for measuring processing [35], with the advantage of speed and simplicity.

A new passive method for visual distance measurement with a single camera is proposed in this paper. It requires a fixed camera and involves the processing of all the images of the object of interest (for each position of the focus lens). In order to overcome the high computational demand of the shape from focus and derived methods, the quality of the image is evaluated globally and not on the pixel granularity level. Since sharpness and contrast define the quality of a perceived image [36,37], a least squares-based sharpness cost function is minimized, yielding the distance to the object of interest.

2. Materials and Methods

2.1. Method Description

The proposed distance measurement method, making use of a least squares-based sharpness cost function, comprises two steps: a calibration step and a measurement one. Calibration is performed only once for a camera type and involves:

- establishing the dependence of the sharpness, for each position of the lens, on the position of the object of interest. A (n,m) mapping matrix is obtained with n and m being the number of the positions of the focus lens and the number of positions of the object of interest, respectively;
- approximating each dependency by a polynomial function S_i and identification of the function coefficients.

Measuring the distance to the object of interest involves:

- taking a set of images of the object (stack) and calculating the sharpness for each position of the lens, $S_{i\_measured}$;
- calculating the Cost Function as being the square deviations between the measured sharpness and the sharpness obtained by calibration for each of the m possible positions of the object;
- $CF(j) = \sum_{i=0}^{n-1} (Si(xj) - Si\_measured)^2$;
- establishing the index of the minimum of the square deviations, which yield the calculated distance;
- $estimated\ index = \min\limits_{j=1;m} CF(j)$.

2.2. Experimental Setup

For testing, the proposed measurement technique used was a Logitech Pro C920 webcam equipped with Carl Zeiss® optics, with a 4-bit focus, equivalent to 16 distinct lens positions. The autofocusing process is completed within a fraction of a second (0.38 s in good light; 0.89 s in low light conditions), set by default responsive, suitable for short or medium distances (this mode is useful when aiming to capture a quick-moving visual task or when aiming to capture multiple visual tasks while switching the focus continually from one to another). The webcam is integrated on an experimental linear displacement stand that allows object movement relative to the camera with a high resolution. Structurally, the stand (Figure 1) is composed of an axis for linear motion with a slider (1), a camera test chart/array of 140 colors (2), a single-ended optical shaft encoder with 0.0235 mm resolution (4096 counts per revolution in quadrature mode/1024 lines per revolution), used for position feedback (3), a DC brushed micromotor, with 0.7 Nm precision planetary gearheads (4), single channel linear voltage-controlled power amplifier (5), a data acquisition board (6) with closed-loop control, connected with (3), and the webcam (7). In order to drive the system toward a target position, a feedback loop with a PID controller is implemented. LabView 2021 software is used for command, control, data acquisition and image processing with Vision Development Module 2021 National Instruments toolkit.

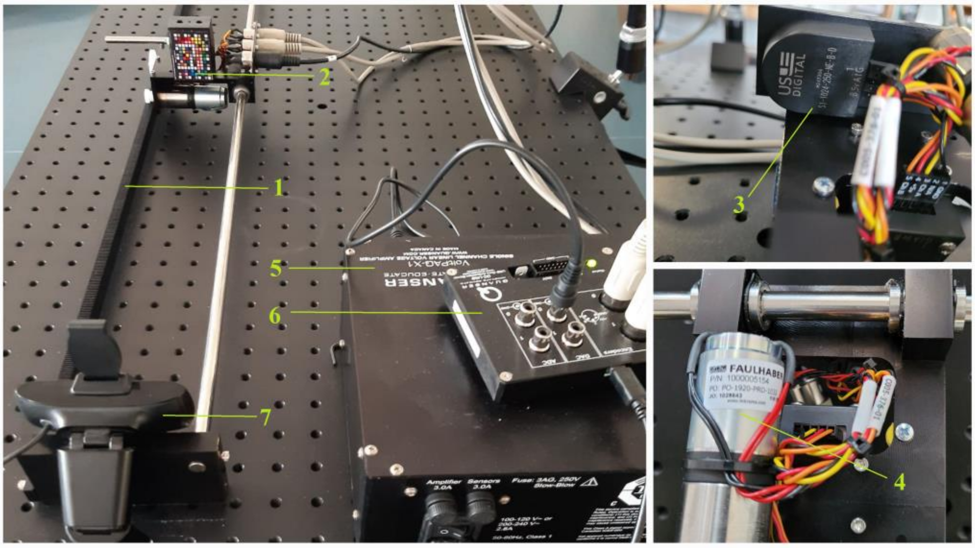

Figure 1. Experimental stand for video distance measurement testing.

3. Results

3.1. Calibration Stage

First, to determine the evolution of the clarities according to displacement, the calibration phase is performed, as rendered in Figure 2. Two cycles are involved: the cycle of the object of interest (1) and the cycle of the focus lens (2). The lens cycle is performed only once for each position (3) of the object cycle and leads to obtaining the image set (stack) on which the focus is established, acquiring the image with the best sharpness. The object cycle involves moving the object of interest (3) along the axis of symmetry of the camera, with a resolution equal to the desired resolution to be obtained when measuring. For each position of the object, the sharpness values (4) obtained from the lens cycle are normalized (5). From the matrix of the obtained data, the dependence of the sharpness on the position of the object (6) is extracted for each position of the lens, and each dependence is polynomially approximated (7).

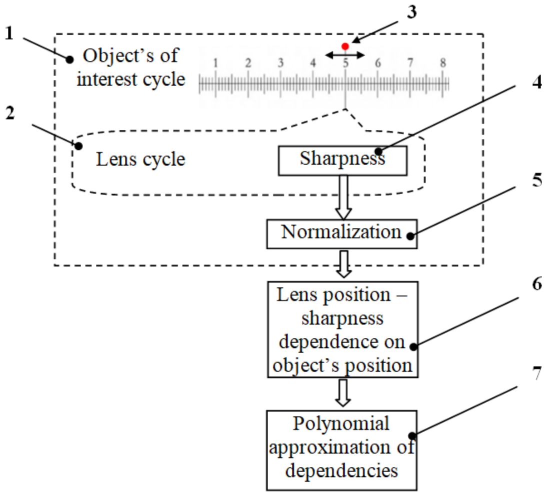

Figure 2. Block diagram of the calibration phase.

From step (6) the dependencies of the sharpness on the position of the object were approximated for each of the 16 positions of the focus lens by a polynomial function:

$$S_i = a_0 + a_1x + a_2x^2 + a_3x^3 + a_4x^4 + a_5x^5 + a_6x^6 \tag{1}$$

where i represents the lens' position, $i = 0 \ldots 15$, x is the objects' position and S_i is the sharpness value. The coefficients of the 16 associated polynomial functions of 6 degree are given in Table 1 and their graphical approximation functions to the data obtained by calibration are rendered in Figure 3. For method accurately accomplishment, all decimals must be used.

Table 1. Polynomial coefficients determined for each lens position.

Lens' Position (i)	**Polynomial Coefficients**						
	a_0	a_1	a_2	a_3	a_4	a_5	a_6
0	1.00242	-3.41879×10^{-3}	-292321×10^{-4}	4.05166×10^{-6}	-2.16663×10^{-8}	5.22761×10^{-11}	-4.74343×10^{-14}
1	0.898721	6.36388×10^{-3}	-4.76928×10^{-4}	5.53824×10^{-6}	-2.7626×10^{-8}	6.40214×10^{-11}	-5.65194×10^{-14}
2	0.802894	1.44673×10^{-2}	-5.99068×10^{-4}	6.25795×10^{-6}	-2.94182×10^{-8}	6.53407×10^{-11}	-5.57859×10^{-14}
3	0.704034	1.85123×10^{-2}	-5.59871×10^{-4}	5.0166×10^{-6}	-2.07422×10^{-8}	4.09188×10^{-11}	-3.11744×10^{-14}
4	0.672847	1.47299×10^{-2}	-3.34911×10^{-4}	2.04935×10^{-6}	-4.44685×10^{-8}	3.8416×10^{-11}	6.60522×10^{-15}
5	0.684477	6.57673×10^{-3}	-2.49564×10^{-5}	-1.41218×10^{-6}	1.24868×10^{-8}	-3.79673×10^{-11}	3.95845×10^{-14}
6	0.707126	-1.54146×10^{-3}	2.0778×10^{-4}	-3.24671×10^{-6}	1.81618×10^{-8}	-4.42197×10^{-11}	3.99154×10^{-14}
7	0.745179	-9.34635×10^{-3}	3.99719×10^{-4}	-4.82945×10^{-6}	2.47073×10^{-8}	-5.8496×10^{-11}	5.28991×10^{-14}
8	0.831732	-2.12925×10^{-2}	6.80613×10^{-4}	-7.49486×10^{-6}	3.79759×10^{-8}	-9.16576×10^{-11}	8.50388×10^{-14}
9	0.706765	-4.9561×10^{-3}	1.48598×10^{-4}	-1.44829×10^{-6}	7.39629×10^{-9}	-1.89172×10^{-11}	1.82406×10^{-14}
10	0.704984	-6.61971×10^{-3}	1.71546×10^{-4}	-1.6138×10^{-6}	7.1569×10^{-9}	-1.44787×10^{-11}	1.04764×10^{-14}
11	0.690874	-4.97126×10^{-3}	1.07935×10^{-4}	-8.17178×10^{-7}	2.66015×10^{-9}	-2.95716×10^{-12}	-3.20389×10^{-16}
12	0.687389	-4.74209×10^{-3}	9.63782×10^{-5}	-6.6829×10^{-7}	1.82623×10^{-9}	-8.70554×10^{-13}	-2.20633×10^{-15}
13	0.682394	-4.54304×10^{-3}	8.85567×10^{-5}	-5.72535×10^{-7}	1.29942×10^{-9}	4.56257×10^{-13}	-3.44156×10^{-15}
14	0.677695	-4.47291×10^{-3}	8.77463×10^{-5}	-5.72904×10^{-7}	1.33118×10^{-9}	3.31304×10^{-13}	-3.29169×10^{-15}
15	0.674817	-4.50933×10^{-3}	8.79664×10^{-5}	-5.6798×10^{-7}	1.27092×10^{-9}	5.60098×10^{-13}	-3.57643×10^{-15}

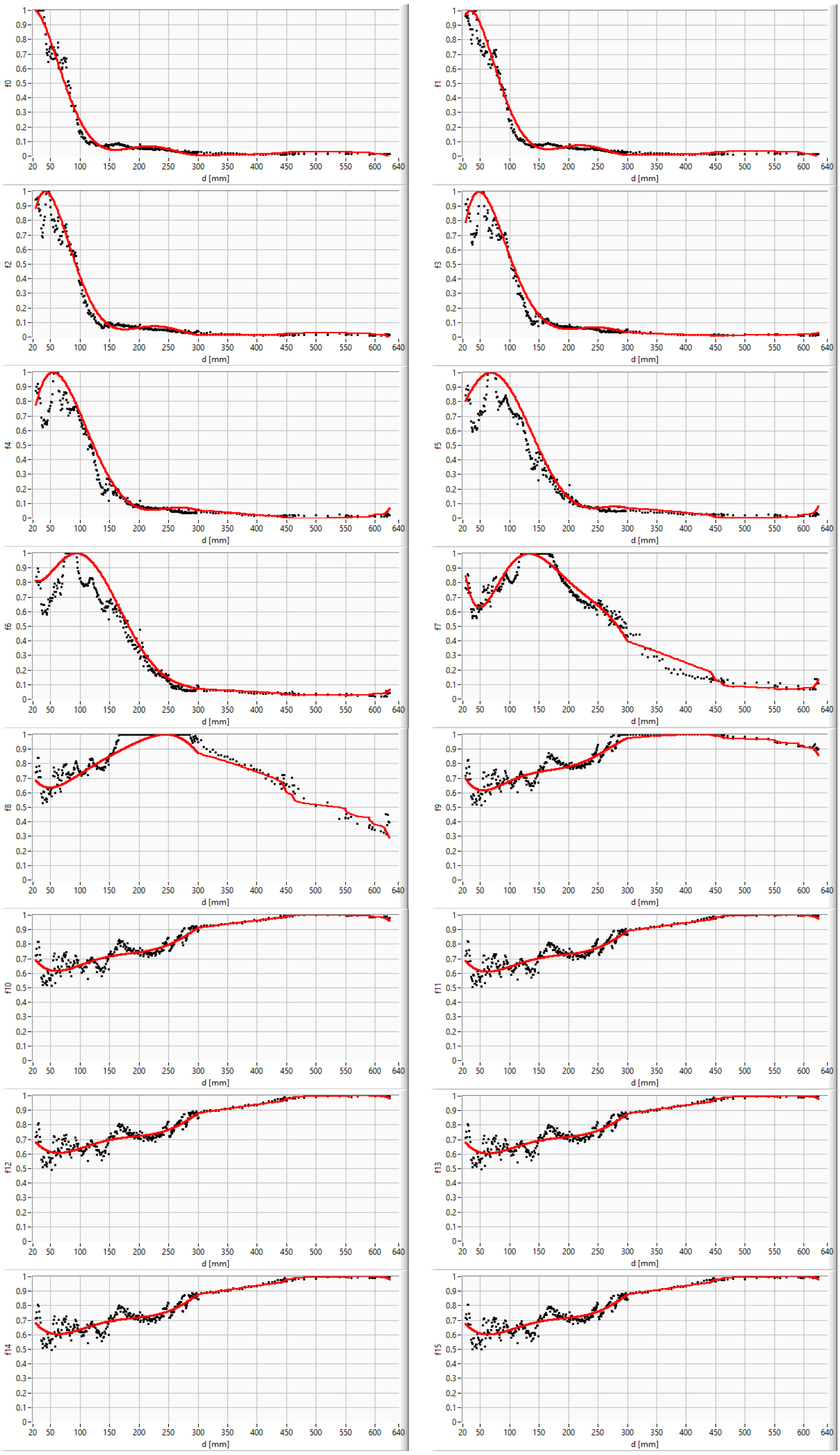

Figure 3. Polynomial approximations of clarities to the position of the object, for each of the 16 focus lens' positions (f_0–f_{15}).

3.2. Measurement Stage

The measurement phase, performed following the operations from Figure 4, involves taking the image set (stack) through the lens cycle (2), calculating the sharpness corresponding to each position of the lens (4) and normalizing the sharpness values (5). Then, one calculates the deviations of the current clarities from the dependencies resulting from the calibration for each position of the object (8), and the index of the minimum deviations is determined (9), which will correspond to the measured distance.

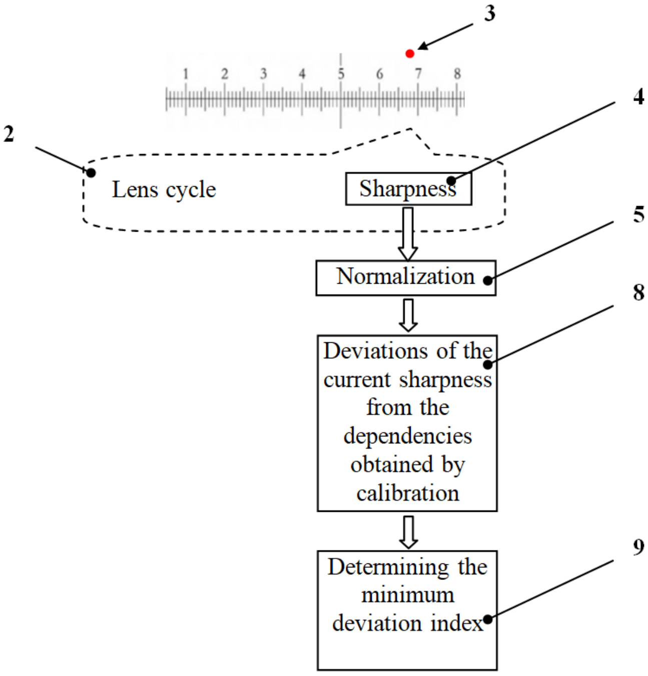

Figure 4. Block diagram of the measurement phase.

For an object placed, for example, at a distance of 104 mm away, the set of 16 images is taken for which the normalized clarities are calculated (Figure 5). For each possible position of the object, the deviation between the current clarities and the ones obtained by calibration is calculated (Figure 6). The minimum deviation is set, which will correspond to a measured distance of 103 mm (Figure 7).

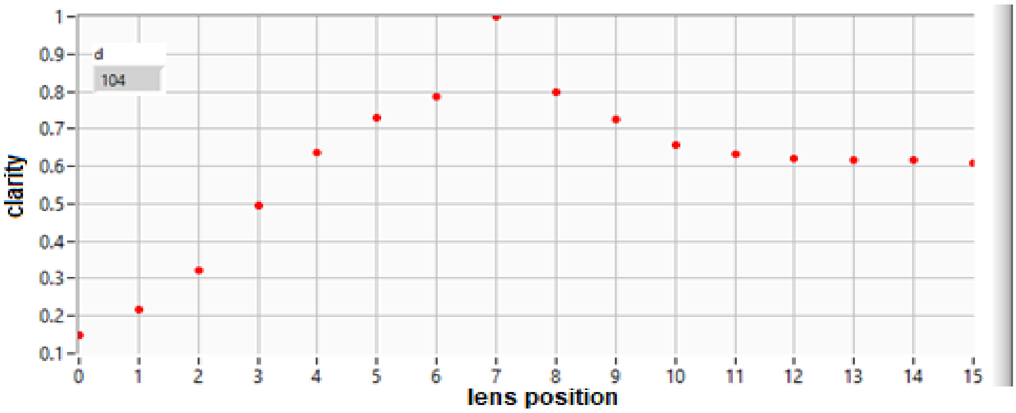

Figure 5. The clarities of a set of images (stack) for an object at 104 mm distance from the camera.

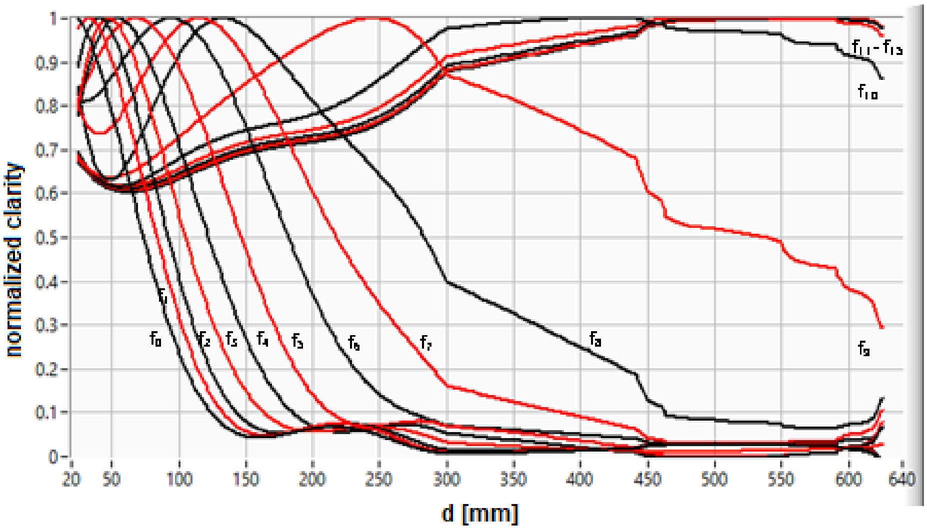

Figure 6. The dependence of the sharpness on the position of the object, for each of the focus lens positions.

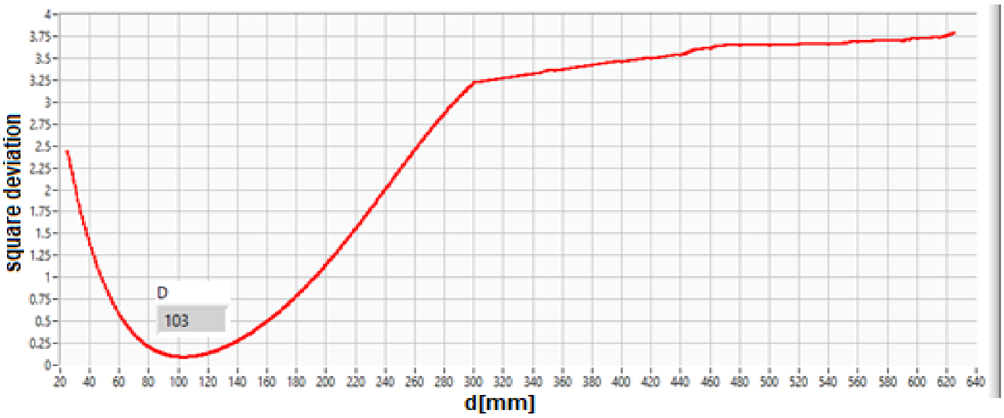

Figure 7. Sharpness cost function for the current measurement (d = 104 mm).

4. Discussion

The object has been displaced in the range of [25 mm; 620 mm], passing through 341 positions. For each position, the relative error was calculated as the difference between the prescribed distance (d) and the distance calculated by the proposed method (D). A graphical render of their values is shown in Figure 8. Moreover, the relative error to the prescribed distance was calculated and displayed in Figure 9.

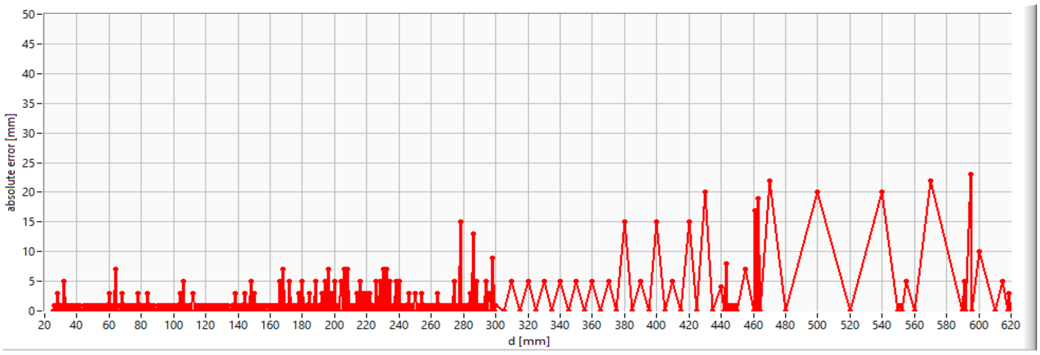

Figure 8. The graphical variation of absolute errors on distance.

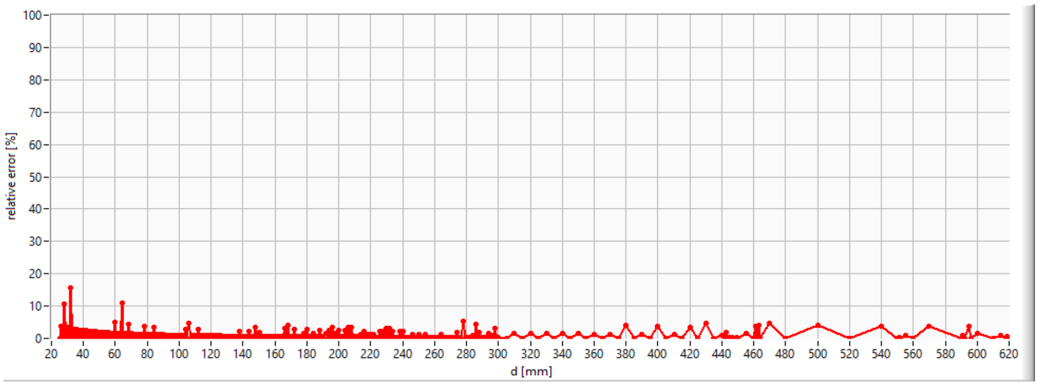

Figure 9. The graphical variation of relative errors on distance.

A qualitative analysis of the obtained results reveals that the relative error falls within a narrow range of values, both for small and large distance values. This is a great advantage when dealing with industrial applications where the measurement range is wide.

A further quantitative evaluation of the reported errors is somehow difficult to be done since there are no established benchmarks for video distance measurement. Moreover, the results are strongly determined by the optical system performance and properties, as highlighted in [38].

A comparative analysis with the best results reported in mainstream publications is presented in Table 2.

Table 2. The relative error in video distance measurement.

Distance [mm]	Zuckerman M., et al. 2017 [39]	Yankin C., et al. 2017 [40]	Hahne C., et al. 2014 [41]	Setyawan R.A., et al. 2018 [42]	Megalingam R.K., et al. 2016 [43]	Dragne C., et al. 2022 [44]	Proposed Method
50					6%		2%
100	23 %				6.3%		1%
150	0.2%				2.7%	10.6%	0.7%
200	7%	1.5%	4.7%		3.5%	2.72%	2.5%
250	7.2%					5.3%	1.2%
300	11%	1.7%	5.9%			6.22%	0.4%
350	7%						1.5%
400	2%						3.7%
450	1.3%	2%	6.7%				0.3%
500	2%			2.5%			4%
550	6.1%						0.3%
600	9%	2.4%	7%	2.1%			1.7%
650	5.3%						

By using the proposed method, improved accuracy is obtained compared to the methods that used dedicated and expensive equipment such as plenoptic (array of microlenses) cameras [40,41] and stereo vision cameras [42,44], or make use of a known dimensional reference in the optical path [43].

5. Conclusions

In this study, a new distance measurement method is proposed, with a single video camera for assessing the distance of an object from the camera. The method comprises a calibration step and a measurement step.

The first step contains the cycle of the object of interest (involving the movement of the object of interest along the axis of symmetry of the camera) and the cycle of the focus lens (performed only once for each position in the object cycle). For each position of the object, the sharpness values obtained from the lens cycle are normalized. The dependence of the sharpness on the position of the object is extracted from the bidimensional data matrix for each lens' position and polynomially approximated.

In the measurement step, for a certain position of the object, a set of images is taken characteristic of the lens cycle, and the sharpness corresponding to each position of the lens is determined and normalized. A least squares-based sharpness cost function is then computed and minimized, yielding the distance to the object of interest.

In terms of accuracy, the proposed method gives similar or better results when compared with reported methods making use of dedicated and expensive equipment such as plenoptic or stereo setups.

Author Contributions: Conceptualization, C.D. and M.C.T.; methodology, M.C.T.; software, C.D.; validation, M.C.T., M.P., C.D. and E.S.; formal analysis, C.D. and M.C.T.; investigation, M.P., M.C.T. and C.D.; resources, C.D. and M.P.; data curation, C.D. and E.S.; writing—original draft preparation, C.D. and M.P.; writing—review and editing, E.S.; visualization, C.D. and E.S.; supervision, E.S.; project administration, M.C.T.; funding acquisition, M.C.T. All authors have read and agreed to the published version of the manuscript.

Funding: This research was funded by European Regional Development Fund, grant number 7386/27.12.2021 (SMIS code 137825)—"Video system for evaluating the standardized dimensions for customers of online clothing stores". The APC was funded by "Gheorghe Asachi" Technical University of Iași, România.

Informed Consent Statement: Not applicable.

Data Availability Statement: Not applicable here.

Conflicts of Interest: The authors declare no conflict of interest. The funders had no role in the design of the study; in the collection, analyses, or interpretation of data; in the writing of the manuscript; or in the decision to publish the results.

References

1. Hamzah, R.A.; Ibrahim, H. Literature survey on stereo vision disparity map algorithms. *J. Sens.* **2016**, *2016*, 8742920. [CrossRef]
2. Zaarane, A.; Slimani, I.; Al Okaishi, W.; Atouf, I.; Hamdoun, A. Distance measurement system for autonomous vehicles using stereo camera. *Array* **2020**, *5*, 100016. [CrossRef]
3. Li, Q.; Chen, G. Fault distance location method of transmission line based on binocular vision technology. In Proceedings of the 7th International Conference on Intelligent Computing and Signal Processing, Xi'an, China, 15–17 April 2022; pp. 1807–1811.
4. Wu, Y.; Shao, S.; Li, Y.; Chen, X.; Che, D.; Chen, J.; Du, K.; Jiang, R.; Huang, X.; Kan, D. Multi-beam optical phase array for long-range LiDAR and free-space data communication. *Opt. Laser Technol.* **2022**, *151*, 108027. [CrossRef]
5. Overview of ARCore and Supported Development Environments. Available online: https://developers.google.com/ar/develop/ (accessed on 9 August 2022).
6. How Does Structure Sensor Work? Available online: https://support.canvas.io/article/7-how-does-structure-sensor-work (accessed on 9 August 2022).
7. Kinovea Features. Available online: https://www.kinovea.org/features.html (accessed on 9 August 2022).
8. Kinect for Windows. Available online: https://docs.microsoft.com/en-us/windows/apps/design/devices/kinect-for-windows (accessed on 9 August 2022).
9. de Arruda Mello, D.A.; Barbosa, F.A. The Optical Transmitter. In *Digital Coherent Optical Systems, Optical Networks*, 1st ed.; Mukherjee, B., Tomkos, I., Eds.; Springer: Cham, Switzerland, 2021; pp. 19–46.
10. Jahid, A.; Alsharif, M.H.; Hall, T.J. A contemporary survey on free space optical communication: Potentials, technical challenges, recent advances and research direction. *J. Netw. Comput. Appl.* **2022**, *200*, 103311. [CrossRef]
11. Tran, T.; Zhang, X. Process monitoring and inspection. In *Digital Manufacturing*; Trombaco, R.G., Ed.; Elsevier: Amsterdam, The Netherlands, 2022; pp. 387–442.
12. Jo, K.; Gupta, M.; Nayar, S.K. SpeDo: 6 DOF ego-motion sensor using speckle defocus imaging. In Proceedings of the IEEE International Conference on Computer Vision, Santiago, Chile, 13–16 December 2015; pp. 4319–4327.
13. Lee, J.; Gupta, M. Blocks-World Cameras. In Proceedings of the IEEE International Conference on Computer Vision and Pattern Recognition, Nashville, TN, USA, 20–25 June 2021; pp. 11412–11422.
14. Zhang, X.G.; Sun, Y.L.; Zhu, B.; Jiang, W.X.; Yu, Q.; Tian, H.W.; Qiu, C.-W.; Zhang, Z.; Cui, T.J. A metasurface-based light-to-microwave transmitter for hybrid wireless communications. *Light Sci. Appl.* **2022**, *11*, 126. [CrossRef]
15. Kirrbach, R.; Faulwaßer, M.; Schneider, T.; Meißner, P.; Noack, A.; Deicke, F. Monolitic Hybrid Transmitter-Receiver Lens for Rotary On-Axis Communications. *Appl. Sci.* **2020**, *10*, 1540. [CrossRef]

16. Nagashima, K.; Ishikawa, Y.; Izawa, A.; Nishita, M.; Matsubara, N.; Ishii, H.; Saeyang, T.; Ogiso, Y.; Ueda, Y.; Kohtoku, M. Transmitter-receiver optical sub assembly using ultra-compact tunable DBR/ring laser. In Proceedings of the IEEE Optical Fiber Communications Conference and Exhibition, Washington, DC, USA, 6–11 June 2021; pp. 1–3.
17. Yang, C.; Huang, X.; Zheng, Y.; Xie, Y.; Duan, X. Non-contact Breathing Rate Detection Based on Time of Flight Sensor. In Proceedings of the 43rd Annual International Conference of the IEEE Engineering in Medicine & Biology Society (EMBC), Guadalajara, Mexico, 1–5 November 2021; pp. 7284–7287.
18. Zhang, X.; Shao, W.; Zhou, M.; Tan, Q.; Li, J. A scene comprehensive safety evaluation method based on binocular camera. *Rob. Auton. Syst.* **2020**, *128*, 103503. [CrossRef]
19. Wu, C.; Yang, L.; Luo, Z.; Jiang, W. Linear Laser Scanning Measurement Method Tracking by a Binocular Vision. *Sensors* **2022**, *22*, 3572. [CrossRef]
20. Xie, Q.; Hu, X.; Ren, L.; Qi, L.; Sun, Z. A Binocular Vision Application in IoT: Realtime Trustworthy Road Condition Detection System in Passable Area. *IEEE Trans. Ind. Inform.* **2022**. [CrossRef]
21. Xiang, H.; Cheng, L.; Wu, H.; Chen, Y.; Gao, Y. Mobile Robot Automatic Aiming Method Based on Binocular Vision. In Proceedings of the 40th Chinese Control Conference, Shanghai, China, 26–28 July 2021; pp. 4150–4156.
22. Wang, Y.; Lai, Z.; Huang, G.; Wang, B.H.; van der Maaten, L.; Campbell, M.; Weinberger, K.Q. Anytime stereo image depth estimation on mobile devices. In Proceedings of the International Conference on Robotics and Automation (ICRA), Montreal, QC, Canada, 20–24 May 2019; pp. 5893–5900.
23. Dai, H.; Zhang, X.; Zhao, Y.; Sun, H.; Zheng, N. Adaptive disparity candidates prediction network for efficient real-time stereo matching. *IEEE Trans. Circuits Syst. Video Technol.* **2021**, *32*, 3099–3110. [CrossRef]
24. Huang, H.; Chen, F.; Cheng, H.; Li, L.; Wang, M. Semantic segmentation guided feature point classification and seam fusion for image stitching. *J. Algorithm Comput. Technol.* **2021**, *15*, 17483026211065399. [CrossRef]
25. Zhou, C.; Yu, H.; Yuan, B.; Wang, L.; Yang, Q. Three-Dimensional Stitching of Binocular Endoscopic Images Based on Feature Points. *Photonics* **2021**, *8*, 330. [CrossRef]
26. Yu, F.; Gallup, D. 3D reconstruction from accidental motion. In Proceedings of the IEEE Conference on Computer Vision and Pattern Recognition, Columbus, OH, USA, 24–27 June 2014; pp. 3986–3993.
27. Im, S.; Ha, H.; Choe, G.; Jeon, H.-G.; Joo, K.; Kweon, I.S. Accurate 3D reconstruction from small motion clip for rolling shutter cameras. *IEEE Trans. Pattern Anal. Mach. Intell.* **2018**, *41*, 775–787. [CrossRef] [PubMed]
28. Im, S.; Ha, H.; Jeon, H.-G.; Lin, S.; Kweon, I.S. Deep Depth from Uncalibrated Small Motion Clip. *IEEE Trans. Pattern Anal. Mach. Intell.* **2021**, *43*, 1225–1238. [CrossRef] [PubMed]
29. Aswini, N.; Uma, S.V. Obstacle avoidance and distance measurement for unmanned aerial vehicles using monocular vision. *Int. J. Electr. Comput.* **2019**, *9*, 3504.
30. Ali, U.; Mahmood, M.T. Robust focus volume regularization in shape from focus. *IEEE Trans. Image Process.* **2021**, *30*, 7215–7227. [CrossRef]
31. Li, Y.; Fu, Y.; Zhong, K.; Ma, B.; Yan, Z. A virtual binocular line-structured light measurement method based on a plane mirror. *Opt. Commun.* **2022**, *510*, 127974. [CrossRef]
32. Gladines, J.; Sels, S.; Blom, J.; Vanlanduit, S. A Fast Shape-from-Focus-Based Surface Topography Measurement Method. *Sensors* **2021**, *21*, 2574. [CrossRef]
33. Vignesh, S.M.; Senthilnathan, R. A Focus-Measurement Based 3D Surface Reconstruction System for Dimensional Metrology. *IOP Conf. Ser. Mater. Sci. Eng.* **2021**, *1012*, 012038. [CrossRef]
34. Nayar, S.K.; Nakagawa, Y. Shape from focus. *IEEE Trans. Pattern Anal. Mach. Intell.* **1994**, *16*, 24–831.
35. Subbarao, M.; Choi, T. Accurate recovery of three-dimensional shape from image focus. *IEEE Trans. Pattern Anal. Mach. Intell.* **1995**, *17*, 266–274. [CrossRef]
36. Asokan, A.; Anitha, J.; Ciobanu, M.; Gabor, A.; Naaji, A.; Hemanth, D.J. Image Processing Techniques for Analysis of Satellite Images for Historical Maps Classification—An Overview. *Appl. Sci.* **2020**, *10*, 4207. [CrossRef]
37. Prajapati, P.; Narmawala, Z.; Darji, N.P.; Moorthi, S.M.; Ramakrishnan, R. Evaluation of perceptual contrast and sharpness measures for meteorological satellite images. *Procedia Comput. Sci.* **2015**, *57*, 17–24. [CrossRef]
38. Skibicki, J.; Golijanek-Jędrzejczyk, A.; Dzwonkowski, A. The Influence of Camera and Optical System Parameters on the Uncertainty of Object Location Measurement in Vision Systems. *Sensors* **2020**, *20*, 5433. [CrossRef]
39. Zuckerman, M.; Kolberg, E. Distance Estimation to Image Objects Using Adapted Scale. *Int. J. Eng. Sci.* **2017**, *6*, 39–50. [CrossRef]
40. Chen, Y.; Jin, X.; Dai, Q. Distance measurement based on light field geometry and ray tracing. *Opt. Express* **2017**, *25*, 59–76. [CrossRef]
41. Hahne, C.; Aggoun, A.; Haxha, S.; Velisavljevic, V.; Fernández, J.C.J. Light field geometry of a standard plenoptic camera. *Opt. Express* **2014**, *22*, 26659–26673. [CrossRef]
42. Setyawan, R.A.; Soenoko, R.; Mudjirahardjo, P.; Choiron, M.A. Measurement accuracy analysis of distance between cameras in stereo vision. In Proceedings of the IEEE Electrical Power, Electronics, Communications, Controls and Informatics Seminar (EECCIS), Batu, Indonesia, 9–11 October 2018; pp. 169–172.

43. Megalingam, R.K.; Shriram, V.; Likhith, B.; Rajesh, G.; Ghanta, S. Monocular distance estimation using pinhole camera approximation to avoid vehicle crash and back-over accidents. In Proceedings of the IEEE 10th International Conference on Intelligent Systems and Control (ISCO), Coimbatore, India, 7–8 January 2016; pp. 1–5.
44. Dragne, C.; Todiriţe, I.; Iliescu, M.; Pandelea, M. Distance Assessment by Object Detection—For Visually Impaired Assistive Mechatronic System. *Appl. Sci.* **2022**, *12*, 6342. [CrossRef]

Measurement 70 (2015) 14–20

Contents lists available at ScienceDirect

Measurement

journal homepage: www.elsevier.com/locate/measurement

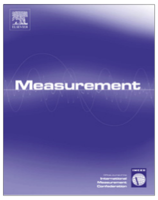

An alternative method to zero-padded DFT

Codrin Donciu [1], Marinel Temneanu *

"Gheorghe Asachi" Technical University of Iasi, Faculty of Electrical Engineering, Bd. Profesor Dimitrie Mangeron, 21-23, 700050 Iasi, Romania

A R T I C L E I N F O

Article history:
Received 12 August 2014
Received in revised form 24 February 2015
Accepted 18 March 2015
Available online 25 March 2015

Keywords:
Discrete Fourier Transform
Zero padding
Picket fence effect

A B S T R A C T

Zero-padding method is usually used to increase the number of points in the DFT and consequently to improve the DFT's approximation of the DTFT. This way the picket fence effect is reduced and a better approximation of DTFT local peaks is achieved for a finite number of measured points. In order to overcome the high computational demand problem of the zero padding method, an alternative one, is further presented in this paper. This method, making use of non-integer number of cycles in DFT kernel orthogonal signals, provide the same results in spectral analysis as zero padding method but with significant reduction of the computational effort. Moreover, the use of non-integer arguments for DFT evaluation open the possibility to develop DFT with variable bins resolution, narrow band DFT and bins interpolation algorithms.

1. Introduction

An accurate spectral analysis of sampled signals, based on Discrete Fourier Transform (DFT), is still a challenge in many scientific areas. Initially, the DFT has not aroused much interest due to its high computational demand but the development of the Fast Fourier Transform (FFT) by Cooley and Tukey [1], endowed the researchers with an efficient tool to compute DFT. Shortly after, the two major drawbacks of their canonical versions, the spectral leakage and the picket fence effect, have been revealed, and their reduction has become the aim of many scientific papers.

The spectral leakage is caused by the algebraic operation performed onto signals with non-integer number of periods, and the only way to completely eliminate the leakage effect is the coherent sampling. However, coherent sampling is difficult to achieve in real world applications and, since spectral leakage is almost inevitable, the windowing technique is used. A general overview of different windows proprieties can be found in [2] and the influence of windows on detection of closely spaced spectral components are provided in [3] where twelve different windows types were investigated.

The picket fence effect (PFE) is a consequence of discrete nature of frequency spectrum, where only binary frequencies (bins) can be evaluated (DFT output) and become observable when the spectral components are not matching the bins. The spectral components parameters are denoted by the peak of its Discrete Time Fourier Transform (DTFT). Taking into account that DFT is computed only in bins, the information regarding peak coordinates will not be exactly achieved. This effect is similar to looking at a fortress through a picket fence.

Two methods are available for PFE reduction: zero padding and bins interpolation. Zero padding represents a solution used to decrease the frequency distance between bins, consisting in lengthening the signal sequence by adding zeroes at the end of time samples, before DFT is applied. However, zero padding does not increase the resolution in the meaning of detection of closely spaced spectral components. Bins interpolation is a parametric method

---

* Corresponding author. Tel.: +40 232 278683.

E-mail addresses: cdonciu@ee.tuiasi.ro (C. Donciu), mtemnean@ee.tuiasi.ro (M. Temneanu).

[1] Tel.: +40 232 278683.

http://dx.doi.org/10.1016/j.measurement.2015.03.015
0263-2241/

based on the evaluation of two or three bins in order to match the peak of DTFT.

Nowadays, combinations between zero padding and different types of interpolation are used to evaluate the spectral components [4,5], as requested in current research areas [6,7], or in comparative studies [8].

However, computing a full zero padded DFT can be wasteful, and advantage should be taken of the inputs that can be discarded. Direct approaches to this problem consist in pruning the flow graph of the complete FFT so as to eliminate the paths corresponding to zero inputs.

Markel [9] was the first to demonstrate the importance in terms of computation reduction that an approach of this type involve. Further on, different algorithms have been proposed in the literature [10–12] in order to reduce the number of multiplications and additions performed in correspondence of the zeros input. The difference in terms of computational complexity among available algorithms was analyzed in [13]. It was shown that all of them are sharing the same objective: to reduce the number of operation $\log_2 M/\log_2 N$ times with N and M representing the number of points in signal and zero padded sequences respectively. However turning these arithmetic gains into actual performance improvements is much more difficult. A pruning matrix has to be defined as to map the distribution of the zero inputs to the FFT block, requiring configuration time and an important space in memory [14].

Moreover, by implementing a pruned FFT, a significant part of the effort that went into optimizing classic FFTs is sacrificed.

Recently, some physical implementation of power aware FFT cores [15] equipped with pruning engine have been reported but with small flexibility in terms of working scenarios.

In order to overcome the high computational demand problem of the zero padding method, an alternative one, is developed in this paper. This method is directly computable by available FFT algorithms and provide the same results (identical spectrums) as zero padding method but with significant computational effort reduction. The target of $\log_2 M/\log_2 N$ ratio of necessary operations is attained without the need of additional pruning matrix or dedicated hardware.

Test performed on an 2nd generation Intel® Core™ i7-2710QE processor based system reveals that for M/N greater than 32, the proposed algorithm is at least twice faster than zero padded FFT.

2. An insight into the zero padding method and bins resolution

The DFT is a mathematical procedure used to determine the spectral components parameters (magnitude, phase and number of cycles) of a discrete signal sequence (a set of discrete values obtained by sampling a time domain continuous signal).

Let us consider a discrete signal $x(n)$ sequence of N points. It is well known that DFT computing represents, for each bin (starting at $k = 0$ and ending at $N-1$ with k integer) the multiplication between DFT kernel and signal sequence:

$$X_k(k) = \sum_{n=0}^{N-1} x(n)e^{-j2\pi nk/N} \tag{1}$$

where k index of $X_k(k)$ represents the kth DFT output component (bin), i.e. $X_0, X_1, \ldots, X_{N-1}$, and k argument represents the number of cycles in kernel functions.

DFT kernel is composed by two discrete orthogonal signals, both with the same number of points as signal sequence. For kernel signals the k argument represents the number of cycles. Accordingly, k represents the number of cycles used by kernel in order to achieve the k bin. Kernel signals are easy observable in DFT rectangular form:

$$X_k(k) = \sum_{n=0}^{N-1} x(n)[\cos(2\pi nk/N) - j\sin(2\pi nk/N)] \tag{2}$$

When analyzing the DFT resolution, there are two items to be considered. The first one is the spectral resolution, referring to the algorithm capability to detect closely spaced spectral components and represent the lowest frequency distance between two closely detectable spectral components (nothing about distance between bins). The second one is bins resolution, representing the distance (in frequency) between to adjacent bins.

While the first one is strictly related to the resolution of the DTFT and can be increased only by increasing the time window of the signal, the second one is determined by the number of points in the DFT. A larger number of bins is usually obtained by using zero padding method, briefly illustrated below.

Assume that a new signal $y(n)$ is created by zero-padding the original $x(n)$ sequence of N points to a length of M points:

$$y(n) = \begin{cases} x(n), & n = 0,\ldots,N-1 \\ 0, & n = N,\ldots,M-1 \end{cases} \tag{3}$$

The M points of the DFT are calculated as:

$$Y_k(k) = \sum_{n=0}^{M-1} y(n)e^{-j2\pi nk/M} \tag{4}$$

Let us consider the non coherent signal sequence $x(n)$ of $N = 100$ points of 2.4 cycles presented in Fig. 1a and its zoom of spectrum in Fig. 1b. (entire spectrum is depicted in Fig. 1c). In order to increase bins resolution, zeroes are added at the end of the original sequence, thus obtaining $y(n)$ sequence (see Fig. 1d). By extending the sequence to $M = 1000$ points, $M - N = 900$ zeroes were added. This process changes the $1/N$ bins resolution into $1/M$ bins resolution. Zoomed spectrum and entire spectrum for M points signal sequence is presented in Fig. 1e and Fig. 1f respectively. For this new $M = 1000$ points sequence, the fundamental bin period is 10 times longer than the previous one.

3. Non-integer argument of DFT

When computing DFT for zero padded sequence, one can notice that the multiplications between kernel orthogonal signals (for $k = 0$ to M) and sequence signal for all samples from $n = N$ to $n = M$ are zero. Thus,

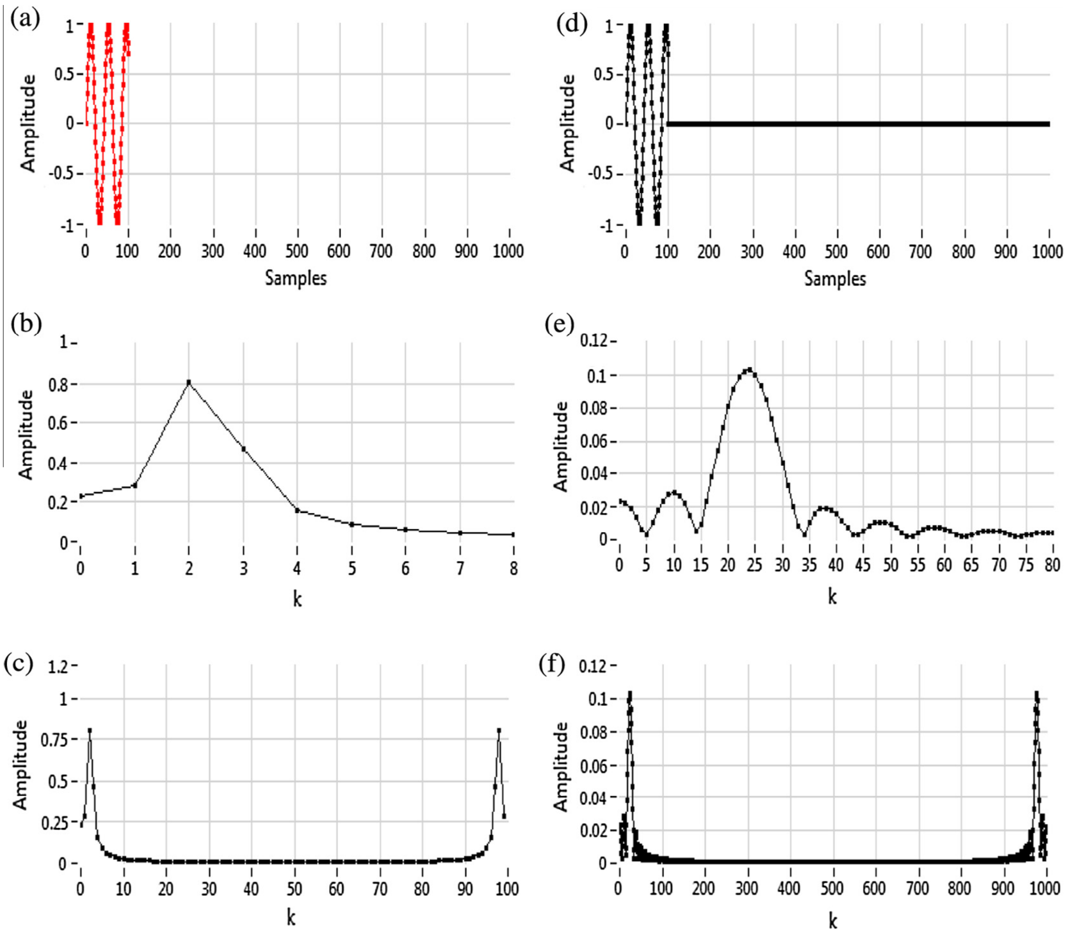

Fig. 1. DFTs of N points sequence and M points zero padded sequence.

$M - N = 900$ irrelevant multiplication for each bins are computed.

This is obvious when performing arrangements on Eq. (4) in order to obtain the relevant and irrelevant sums respectively:

$$Y_k(k) = \sum_{n=0}^{N-1} y(n)e^{-j\frac{2\pi nk}{M}} + \sum_{n=N}^{M-1} y(n)e^{-j\frac{2\pi nk}{M}} \tag{5}$$

Since $y(n)$ is zero for $n = N, \ldots, M - 1$

$$Y_k(k) = \sum_{n=0}^{N-1} y(n)e^{-j\frac{2\pi nk}{M}} \tag{6}$$

It is the moment to assume that k index and k argument have different meanings and consequently can have different values. With $k' = k\frac{N}{M}$, Eq. (6) becomes:

$$Y_k(k') = \sum_{n=0}^{N-1} y(n)e^{-j\frac{2\pi nk'}{N}} \tag{7}$$

Or, more familiar:

$$X_k(k') = \sum_{n=0}^{N-1} x(n)e^{-j\frac{2\pi nk'}{N}} \tag{8}$$

with $k = 0, \ldots, M - 1$.

Now, forget that we started this simple mathematical arrangement from a zero padded sequence. Eq. (8) can be rephrased by: Being a discrete signal $x(n)$ sequence of N points one can obtain $M > N$ frequency bins simply by computing DFT for non-integer arguments.

This is the very essence of the proposed algorithm, with the following additional remarks:

- both zero padding method and the proposed algorithms share the same objective: to increase bin's resolution and consequently to reduce the picket fence effect. None of this methods increase the spectral resolution which is strictly related to the resolution of the DTFT;
- the obtained results are the same but the computational effort is significantly reduced when using the proposed algorithm. With some minor modifications of the existing FFT algorithms, allowing the kernel to have non-integer value of k, it is possible to compute M bins DFT in $O(M\log_2 N)$ instead of $O(M\log_2 M)$ when using zero padded method.
- when the whole spectrum of the signal is not the subject of interest, one can directly evaluate the content of a narrow frequency band.

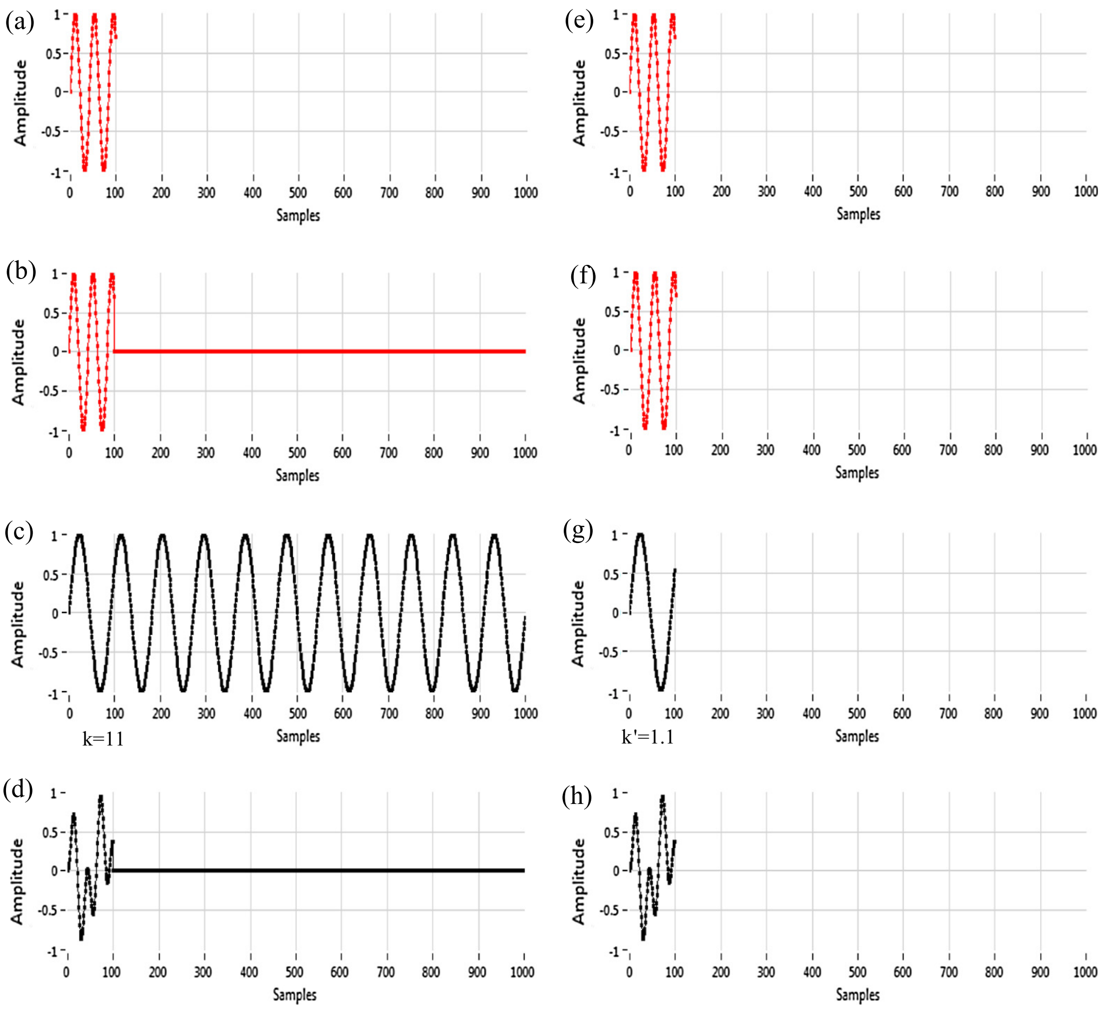

Fig. 2. Two different ways for the same result.

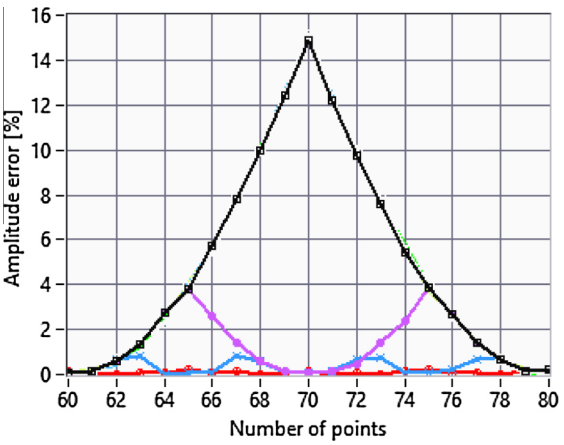

Fig. 3. Relative error of amplitude estimation for different lengths of input sequence.

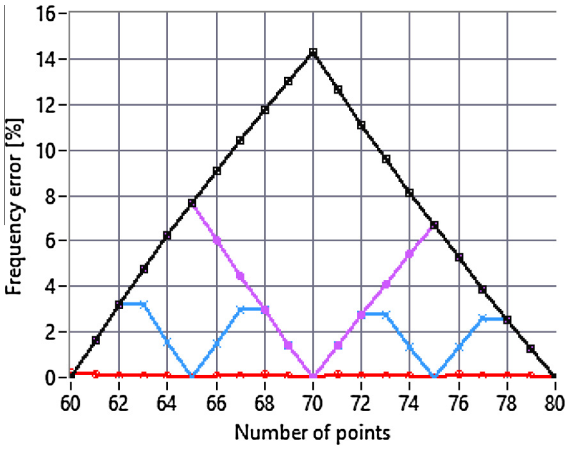

Fig. 4. Relative error of frequency estimation for different lengths of input sequence.

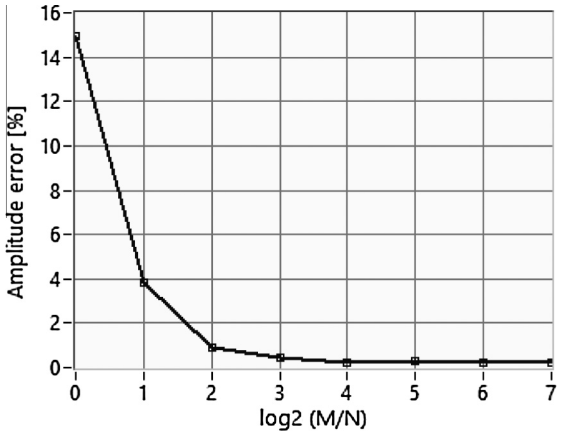

Fig. 5. Maximum relative error of amplitude estimation for different M/N ratio.

- the use of non-integer arguments for DFT gives the opportunity to perform DFT with variable bins resolution.

In order to emphasize the similarity between the results obtained by zero padding method and those obtained with the proposed algorithm, the same numerical example as the one used when illustrating the mechanism of zero padded method will be discussed.

Let $x(n)$ be a non coherent signal sequence of $N = 100$ points. If interested in obtaining $M = 1000$ frequency bins two approaches are available now:

(a) The classic approach consisting in zero padding the $x(n)$ sequence to a length of 1000 by adding 900 zero valued points. The frequency bins are then evaluated by:

$$Y_k(k) = \sum_{n=0}^{999} y(n) e^{-j2\pi nk/M} \tag{9}$$

with $k = 0; 1; \ldots; 999$.

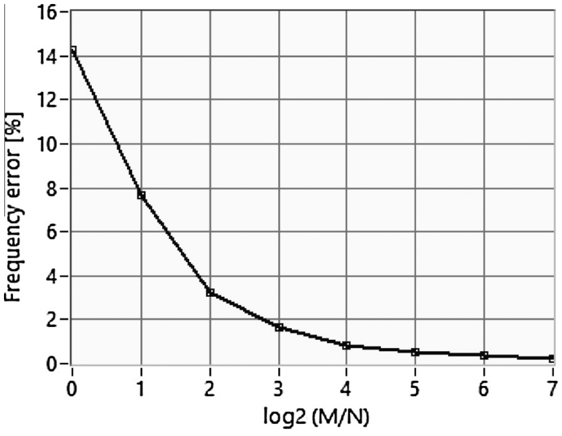

Fig. 6. Maximum relative error of frequency estimation for different M/N ratio.

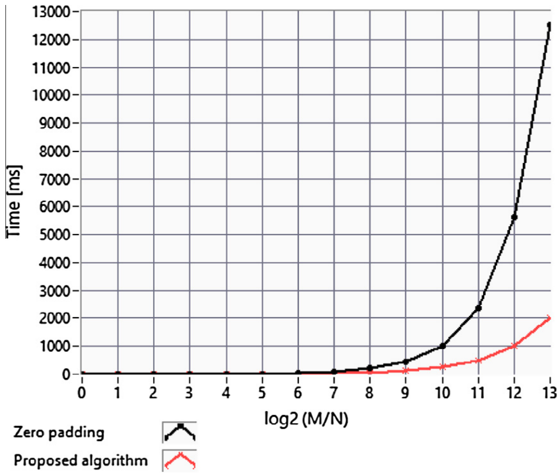

Fig. 7. Execution time for zero padded FFT and proposed algorithm, for $N = 128$.

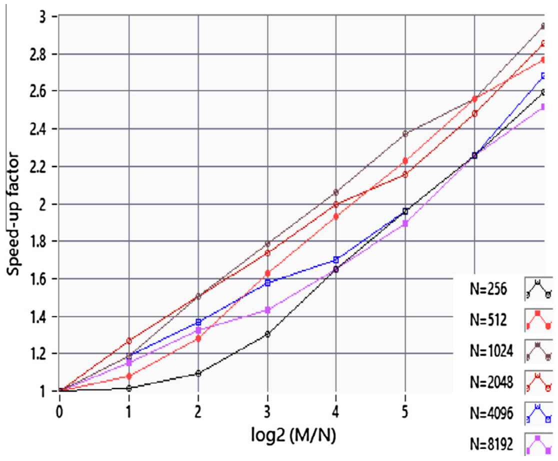

Fig. 8. Speed-up factor for different lengths of input sequences.

(b) The approach proposed in this paper consisting in the evaluation of the DFT formula with non-integer arguments. Since $N = 100$ and $M = 1000$, the distance between two consecutive arguments is $N/M = 0{,}1$ instead of being 1 (classic approach). The frequency bins are evaluated by:

$$X_k(k') = \sum_{n=0}^{99} x(n) e^{-j\frac{2\pi nk'}{N}} \tag{10}$$

with $k = 0; 1; \ldots; 999$ and $k' = 0; 0.1; \ldots. 99.9$.

An illustration of the result obtained for an arbitrary selected bin is depicted in Fig. 2.

The multiplication process performed over the zero padded sequence $y(n)$ is presented in the left column. Following the signal sequence (Fig. 2a), in the left column is presented the zero padded sequence for $M = 1000$ (Fig. 2b) and the $k = 11$ kernel signal (Fig. 2c). The resulted signal after multiplication is presented in Fig. 2d. All the samples from $n = N$ to $M - 1$ are zeroes and becomes irrelevant for DFT sum.

In the right column of are represented the signals obtained by applying the DFT formulas over the original $x(n)$ signal sequence with k' taking a non-integer value ($k' = 11 * N/M = 1.1$).

From the spectrum point of view both the left and right signals are producing the same spectrum. But when evaluating the computational demand the things look different, a larger number of operations being performed by zero padding DFT.

Finally, it arrives that using zero padding method is equivalent with using a non-integer argument. So the question arises: why not use this non-integer argument from the very beginning?

4. Experimental results

Since in most applications DFT processing takes too long, DFT is usually computed using the Fast Fourier Transform (FFT). Therefore, a modified Real to Complex FFT source, allowing the kernel to have non-integer values of k, has been developed in order to evaluate the performances of the proposed algorithm.

Assuming that the length of the signal sequence is N and $M > N$ bins are required, the results of the following approaches have been compared:

- classic Real to Complex FFT applied for the padded sequence – $O(M \log_2 M)$ operations.
- Modified FFT, applied M/N times for the N points sequence – $O(M/N * N \log_2 N) = O(M \log_2 N)$ operations.

The test procedure comprises two stages.

In the first one, the accuracy of the proposed algorithm was tested, in terms of relative error in amplitude and frequency estimation. For this purpose, a 50 Hz signal from a signal generator was acquired through a data acquisition board and sampled at 1 kHz. The work reported in this paper concerns the picket fence effect and therefore a standard Hanning window was applied to the resulting signal to mitigate the influence of the spectral leakage. Further, the relative error in amplitude and frequency estimation was determined by using both classic and modified FFT. Since these errors are strongly dependent on the coherence of the input signal, a complete analysis was performed from $N = 60$ to $N = 80$ points, corresponding to an evolution of the signal from 3 to 4 acquired cycles. The results obtained for $M/N = 1$; 2; 4 and 128 are presented in Figs. 3 and 4.

As expected, both classic and proposed FFT algorithms are performing very well when an integer number of cycles is acquired ($N = 60$ and $N = 80$). Unfortunately, the frequency of the input signal is usually unknown and an arbitrary chosen number of samples can lead to significant errors. Therefore the maximum error has to be considered. As shown in Fig. 3, the amplitude error decrease from 15% (classic FFT with $N = 70$ – corresponding to 3.5 cycles) to 4% (proposed FFT $M/N = 2$), 0.7% ($M/N = 4$) and 0.065% ($M/N = 128$). Similar results are obtained when estimating the frequency of the input signal.

In order to emphasize this behavior, in Figs. 5 and 6 are represented the evolution of the maximum relative error of the amplitude and frequency estimations for different M/N values.

In the second stage of the test procedure, the computational effort of the proposed algorithm was evaluated and compared with the one requested by zero padded FFT, the closest algorithm in terms of accuracy performances.

This stage comprises the following steps:

- Seven discrete signal sequences of N points ($N = 128$, 256, 512, 1024, 2048, 4096 and 8192) have been generated.
- The execution time of classic FFT for each of these sequences has been recorded, together with the execution time for each of these sequences, padded with zeroes up to, at least, $M/N = 128$.

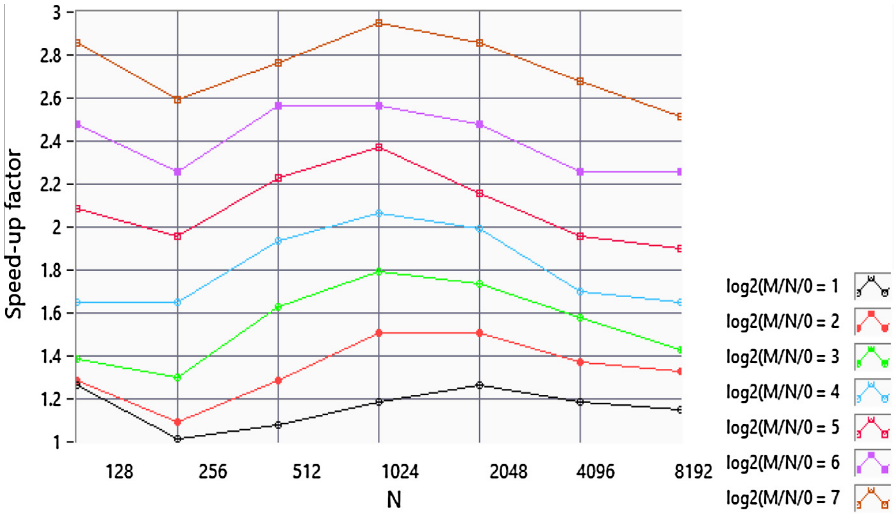

Fig. 9. Speed-up factor for different M/N ratios.

– The same FFT source, modified to admit non-integer values of k as argument has been used to obtain the same bin's resolutions as the ones obtained by zero padding.

The results obtained on a platform based on a 2nd generation Intel® Core™ i7-2710QE processor are presented in Figs. 7–9.

In Fig. 7, the execution time for an input sequence with $N = 128$ and M/N up to 2^{13} is represented for both zero padded and modified FFT. The experimental plots are not strictly correlated with the number of FFT operations but the speed-up factor, evaluated as the ratio of zero padded FFT and the modified FFT is significant. In Fig. 8 this parameter is plotted for the rest of the test sequences. It reveals that for M/N greater than 32, the proposed algorithm is at least twice faster than zero padded FFT.

Maximum gain in terms of speed-up factor is obtained for input sequences with 512–2048 samples, as resulting from Fig. 9.

5. Conclusion

The proposed algorithm allows the calculation of an increased number of DFT bins by straightforward evaluation of the DFT formulas for non-integer arguments. The results, in terms of bins resolution, are similar with those obtained by using zero padded method. With some minor modifications of the existing FFT algorithms, allowing the kernel to have non-integer value of k, it is possible to compute M bins DFT in $O(M\log_2 N)$ instead of $O(M\log_2 M)$ when using zero padded method.

Even if the experimental determined execution time is not strictly correlated with the number of FFT operations the speed-up factor of the proposed method is significant, for M/N greater than 32 the proposed algorithm being at least twice faster than the zero padded FFT.

Moreover, the use of non-integer arguments for DFT evaluation open the possibility to develop DFT with variable bins resolution, narrow band DFT and bins interpolation algorithms.

Acknowledgement

This work was supported by a Grant of Romanian National Authority for Scientific Research, CNDI-UEFISCDI, project TexVidAssist, 251_PCCA_2014.

References

[1] J.W. Cooley, J.W. Tukey, An algorithm for the machine calculation of complex Fourier series, Math. Comput. 19 (1965) 297–301.

[2] F.J. Harris, On the use of windows for harmonic analysis with the Discrete Fourier Transform, Proc. IEEE 66 (1) (1978) 51–83.

[3] M. Novotny, M. Sedlacek, The influence of sidelobes on DFT-based multifrequency signal measurement, Comput. Stand. Interface 32 (3) (2010) 110–118.

[4] B.G. Quinn, Recent advances in rapid frequency estimation, Digit. Signal Process. 19 (6) (2009) 942–948.

[5] J. Borkowski, J. Mroczka, LIDFT method with classical data windows and zero padding in multifrequency signal analysis, Measurement 43 (10) (2010) 1595–1602.

[6] S. Jawla, J.P. Hogge, S. Alberti, Theoretical investigation of iterative phase retrieval algorithm for quasi-optical millimeter-wave RF beams, IEEE Trans. Plasma Sci. 37 (3) (2009) 403–413.

[7] S. Oh, H.J. Kong, E.K. Choi, H.C. Kim, Y.S. Choi, Complex fractionated electrograms and AF nests in vagally mediated atrial fibrillation, Pacing Clin. Electrophysiol. 33 (12) (2010) 1497–1503.

[8] H.S. Pang, B.M. Jeon, On the window selection for three FFT-based high-accuracy frequency estimation methods, IEICE Trans. Fund. Electron. Commun. Comp. Sci. E88A (5) (2005) 1365–1368.

[9] J.D. Markel, FFT Pruning, IEEE Trans. Audio Electro Acoust. 19 (4) (1971) 305–311.

[10] D.P. Skinner, Pruning the decimation in-time FFT algorithm, IEEE Trans. Acoust. Speech Signal Process. 24 (2) (1976) 193–194.

[11] R. Stasinski, FFT pruning. A new approach, Proc. Eusipco 86 (1986) 267–270.

[12] H.V. Sorensen, C.S. Burrus, D.L. Jones, A new efficient algorithm for computing a few DFT points, Proc. of the IEEE Int. Syrup. on CAS (1988) 1915–1918.

[13] Y. Xu, C.H. Lee; M.S. Lim, Design of split-radix FFT pruning for OFDM based cognitive radio system, in: Circuits and Systems (APCCAS), 2010 IEEE Asia Pacific Conference on, pp. 2010, 524–527.

[14] Y. Xu, D. Kim, S. Lee, M.S. Lim, Split-radix FFT pruning for OFDM based cognitive radio system, in: Communications and Information Technology, 2009, ISCIT 2009. 9th International Symposium on, 2009, pp. 421–424.

[15] R. Airoldi, F. Campi, M. Cucchi, D. Revanna, O. Anjum, J. Nurmi, Design and implementation of a power-aware FFT core for OFDM-based DSA-enabled cognitive radios, J. Signal Process. Syst. Arch. 78 (3) (2015) 257–265.

2014 International Conference and Exposition on Electrical and Power Engineering (EPE 2014), 16-18 October, Iasi, Romania

Appliance Characterization Based on Spectral Components Analysis

Marinel Temneanu
Faculty of Electrical Engineering
“Gheorghe Asachi” Technical University of Iaşi
Iaşi, România
mtemnean@ee.tuiasi.ro

Abstract—**Appliance detection within the total load can offer the user a better understanding of how the energy is used and can help him find solutions to reduce consumption and costs. The detection can be made based on the specific electrical signature each one has. This paper presents a new algorithm which characterize the appliances by making use of some parameters obtained from the spectral analysis of the electrical current. The obtained electrical signature is characterized by a large number of parameters which help distinguish similar appliances from each other.**

Keywords: electrical signature; nonintrusive load monitoring; appliance detection; spectral analysis

I. INTRODUCTION

The disaggregation of energy consumption into individual appliances represents an important research direction as it can provide solutions that can be used to reduce the energy consumption. Information regarding the consumption of electrical devices helps reducing the energy consumption by providing customized solutions for different locations or situations (householding or maintaining a business): it can be used to identify which appliances (HVAC systems or electronics) could most effectively reduce the consumption of energy[1]. According to some studies, the consumption of energy can be reduced up to 12% by using the appliance feedback [2-3]. The appliance feedback can provide users useful information which could help them identify solutions to reduce the energy consumption [4]: they can detect appliances with the biggest percentage of the total energy consumption, making them think about replacing those appliances with more effective ones, or seize opportunities to shift different activities to off-peak hours when the energy costs are lower. Virtual instruments, which are used in various areas [5-7], can be implemented to provide a more user-friendly interface.

The techniques used to disaggregate the energy consumption into individual appliances can be classified into two categories: intrusive and nonintrusive. The first ones use monitoring devices, connected to each appliance, which send information about the consumption to a central unit, while the second one uses a single monitoring device which, by analyzing different electrical parameters, can detect and monitor the consumption of the appliances connected to the power network. The second technique, also known as nonintrusive load monitoring (NILM), presents the advantage of a simple architecture which doesn’t require high costs. In spite of that, a complex software component is needed. Usually it monitors the voltage and current signals at the entrance point of the electrical network and it extracts different parameters, whose variations can be correlated to the operating status of the appliances connected to the network. These parameters, which can describe the status of and appliance, represent the electrical signature. Depending on when are these parameters detected, there can be three types of signatures distinguished: steady-state signatures [8-13], transient signatures [14-17] or a combination of both [18-20].

Over the years different parameters were used by the researchers to characterize an appliance’s electrical signature. The most common analyzed parameters are the active and reactive powers that underlie the NILM technique. Their step changes were first used by G.W. Hart to observe what was happening in a house in terms of appliance using [21]. Using finite state machines an appliance could be characterized through its whole operating cycle. Besides the step changes, the transient profiles of the two powers generated when an appliance is switched from one state to another, were also used for detection [17]. The transient profiles were characterized by a series of parameters, such as duration, number of transitions and total power change.

The non linear loads draw currents of harmonics frequencies, whose values can also be used to characterize the electrical signature [13],[22-23]. The harmonic content can also be used to detect and extract those consumers with a variable consumption from the total load. It was found that certain correspondences can be obtained between fundamental and different harmonic components [24-25].

Most of the modern electronics use switched mode power supplies to achieve a higher efficiency. This however comes with a cost which is the high frequency electromagnetic interferences generated by these power supplies. A group of researchers exploited this issue and used these interferences (noises) to detect the presence of an appliance [14],[16]. The method consisted in performing a spectral analysis on the detected noises and comparing the results with the ones recorded in a database in order to identify an appliance. These signals can be analyzed using different techniques such as wavelet or Wigner functions [26-27].

978-1-4799-5849-8/14/$31.00 ©2014 IEEE

A different approach of detecting the operating status of an appliance consisted in using different types of sensors. For example, in [28], electromagnetic field sensors were used to detect the operating status of the appliances, by sensing the electric and magnetic fields generated by those appliances. This information, correlated with the total power consumption can help a NILM system to improve the detection process. In [29], a combination of magnetic, light and acoustic sensors was used to detect the electrical consumers. The magnetic sensor, placed near the power cord, was used to monitor the current which would be further used to determine the power consumption, while the acoustic and light sensors were used to detect the internal power state of the appliances.

In this paper we present an algorithm which characterizes the appliance's electrical signatures based on a steady-state analysis of the current’s harmonics and phases. The algorithm detects the events generated by the appliances switching from one state to another. When the steady-state occurs, it extracts a segment of the electrical current signal. This segment is subtracted from the segment characteristic to the previous steady-state and the resulting signal is the subject of a spectral analysis in order to determine the parameters of interest.

II. ALGORITHM DESCRIPTION

The algorithm uses the voltage and current signals to continuously monitor the active and reactive powers which will be used to detect events that can be assigned to an appliance switching from one state to another. The detection of an event occurs when the active power’s variation exceeds a certain threshold. When this happens, the algorithm will extract the voltage and current waveforms of the appliance that determined the event, by subtracting the waveforms acquiered before and after the event. The resulted data segment (current waveform) will be further processed in order to compute the electrical signature’s parameters.

Since the electrical signature is consisted of current’s harmonics and phases, which depend on the shape and phase of the acquired segment, it is therefore essential to bring the data segment to a predefined state. This is achieved by subtracting a sub-segment whose phase is as close as possible to a predefined value. The procedure by which the sub-segment is extracted is performed in two stages which are presented below.

In the first stage, the phase resolution $d\phi$ is determined, depending on the current’s frequency and the sampling frequency. This parameter indicate us how many degrees correspond to the interval between two successive samples. Knowing the signal’s frequency f_s and the sampling frequency f_e, the number of samples N_{per} corresponding to a period of the signal is:

$$N_{per} = \frac{f_e}{f_s}. \tag{1}$$

Since a period has 360°, the phase resolution is given by:

$$d\phi = \frac{360}{N_{per}}. \tag{2}$$

Knowing the phase resolution and the initial phase of the data segment, the number of samples after which the signal’s phase is in the vicinity of the imposed value is estimated. begining with this estimation the algorithm passes on to the second stage, which aims to improve the accuracy of estimating the imposed phase. The algorithm determines the phases of a sub-segment estimated in the first stage (ϕ_e) and for other two sub-segments obtained by adding (ϕ_{e+1}) respectively extracting (ϕ_{e-1}) one sample. The phase estimation is achieved by using the DFT algorithm based on variable frequency resolution, concept presented in [30-31]. After that, the values of the estimated phases are compared with the imposed one and the closest one is selected. If the selected phase is ϕ_e, then is considered that the required precision is achieved. Otherwise, the process is repeated by adding or extracting one sample from the selected sub-segment, until a minimum difference is obtained between the imposed phase and the estimated one.

Once the sub-segment whose phase is in the vicinity of the imposed one is extracted, the current’s signal corresponding to the detected event is determined. This is achieved by subtracting the sub-segments recorded before and after the event. The difference thus obtained will represent the signal which corresponds to the appliance that generated the event. Using the extracted signal, the phases and magnitudes of the current’s harmonics are estimated and, together with the active power, will represent the electrical signature of an appliance. These values will be recorded in a database which will be further used to detect the appliances present in a house.

III. RESULTS AND DISCUSSIONS

Using the algorithm presented in the previous section, a number of 47 appliances which are usually found in a house were investigated to determine their electrical signatures. The signatures were recorded in a database which contains resistive, inductive loads or appliances that use switched mode power supplies. Depending on the availability, different batches for the same product were analyzed in order to observe the repeatability of the electrical signatures.

There can be appliances with different operating states, a category that includes consumers with a variable load (a drilling machine has a different consumption depending on the composition of the material which is drilled) or consumers that perform different functions (the washing machine: water pumping, water heating, drum rotation and centrifugation). For these consumers the electrical signatures for different loads and functions were determined. This way the operating states of these consumers could be detected.

In the figures bellow, the electrical signatures of a number of representative appliances will be presented, considering 0° the value of the imposed phase. In the left column the current’s characteristics are presented while in the right column the voltage characteristics.

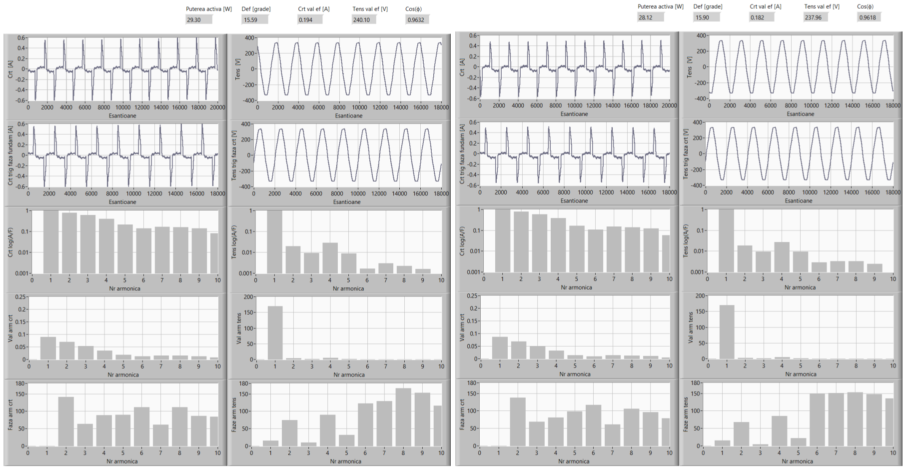

Puterea activa [W] 29.30
Def [grade] 15.59
Crt val ef [A] 0.194
Tens val ef [V] 240.10
Cos(ϕ) 0.9632

Puterea activa [W] 28.12
Def [grade] 15.90
Crt val ef [A] 0.182
Tens val ef [V] 237.96
Cos(ϕ) 0.9618

a. b.

Figure 1. Electrical signatures of a 17 inch LCD monitor: a. lot I, b. lot II

In the first line are presented the data segments acquired when an event is detected, in the second line the extracted sub-segments with the imposed phase, in the third line the values of the odd harmonics (A, up to 19th order) normalized to the fundamental F in a logarithmic scale, in the fourth line the harmonics in a linear scale and in the fifth line the values of the harmonics' phases. Also in the upper part can be observed the active power, phase shift, current and voltage values and $\cos\phi$.

In Fig. 1 is presented a comparison between the electrical signatures of two lots of the same appliance, a 17 inch LCD monitor. It can be observed from the two signatures that the harmonics' amplitudes and phases present similar values for both of the lots. The harmonics' amplitude presents a descending trend for both lots, starting from a 0.09 A value of the first order harmonic and ending with a value of 0.02 A of the 19th harmonics. The phase of the first order harmonic (fundamental) takes the value of the imposed phase, 0°. The values of the rest of the phases vary between 60° and 140°, and are similar for both lots. Also the active powers are 29.3 W for the first lot and 28.12 W for the second.

In Fig. 2 is presented the electrical signature of the two operating states of an air conditioner unit (AC), heating and cooling. By comparing the harmonics' amplitudes for the two states it can be observed that the fundamental component has a value of 2.7 A for the heating state and 1.8 A for the cooling state. Differences can also be observed when the phases are compared. The active power for the heating state is 900.82 W while the one of the cooling state is 565.32 W.

In Fig. 3 we observe the electrical signatures of two resistive appliances, an iron and a toaster. The fact that the two appliances are resistive can be observed by analyzing the normalized harmonics and their phases. As it is known, resistive loads will draw a current with the same waveform as the voltage. In the case presented in Fig. 3, it can be seen that the normalized values of the current harmonics have the same values as the ones of voltage harmonics – the proportions between the fundamental and harmonics is the same both for current and voltage.

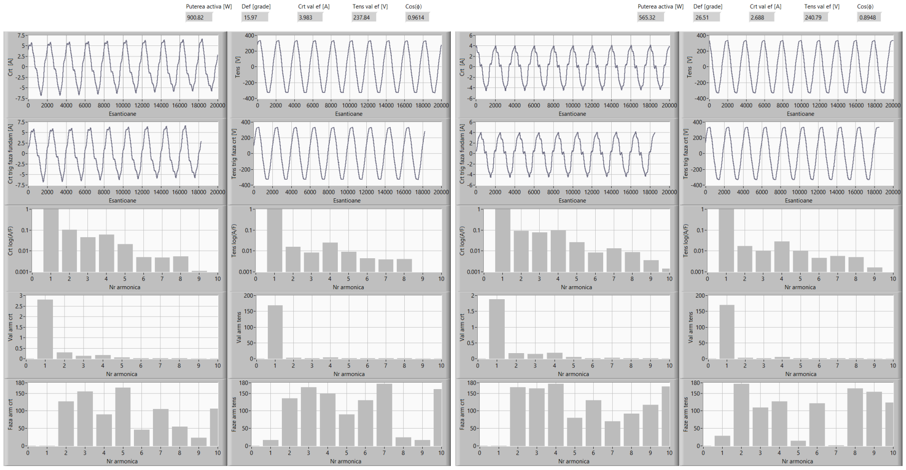

Puterea activa [W] 900.82
Def [grade] 15.97
Crt val ef [A] 3.983
Tens val ef [V] 237.84
Cos(ϕ) 0.9614

Puterea activa [W] 565.32
Def [grade] 26.51
Crt val ef [A] 2.688
Tens val ef [V] 240.79
Cos(ϕ) 0.8948

a. b.

Figure 2. Electrical signatures of the states of an AC unit: a. heating, b. cooling.

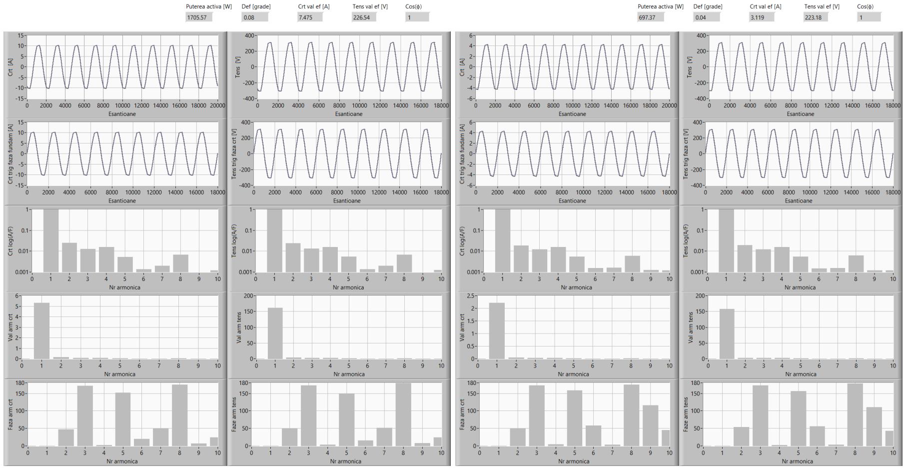
Puterea activa [W] 1705.57
Def [grade] 0.08
Crt val ef [A] 7.475
Tens val ef [V] 226.54
Cos(ϕ) 1

Puterea activa [W] 697.37
Def [grade] 0.04
Crt val ef [A] 3.119
Tens val ef [V] 223.18
Cos(ϕ) 1

a. b.

Figure 3. Electrical signatures of: a. iron, b. toaster

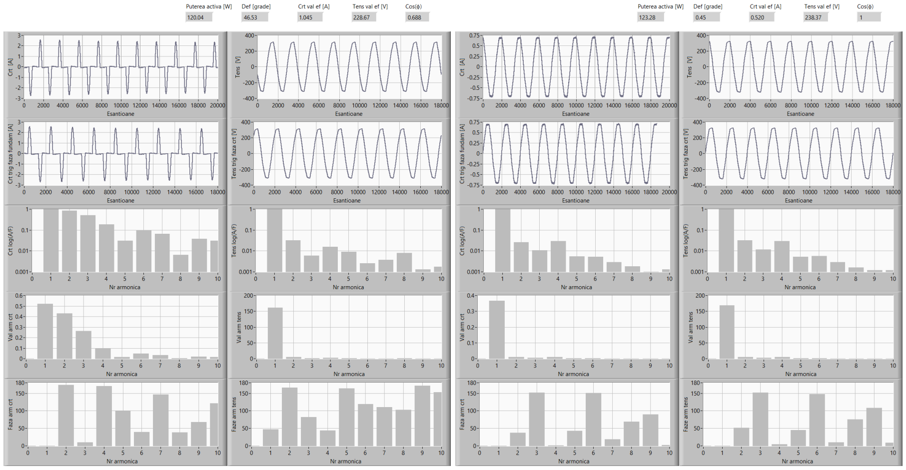
Puterea activa [W] 120.04
Def [grade] 46.53
Crt val ef [A] 1.045
Tens val ef [V] 228.67
Cos(ϕ) 0.688

Puterea activa [W] 123.28
Def [grade] 0.45
Crt val ef [A] 0.520
Tens val ef [V] 238.37
Cos(ϕ) 1

a. b.

Figure 4. Electrical signatures of: a. juicer, b. incandescent light bulb

Also, it can be observed that the phases of current harmonics and voltage harmonics are the same. The difference between the two appliances can be seized when the values of the harmonics represented in a linear scale are compared. Since the two appliances are of different powers, the current's fundamental will also have different values: 5.2 A for the iron and 2.2 A for the toaster. The active powers are 1705.57 W for iron and 697.37 for toaster.

In Fig. 4 is presented a comparison between two appliances of similar powers, juicer (120.04 W) and incandescent light bulb (123.28 W). Although they could be considered as a single appliance when comparing the active powers, when the amplitudes and phases of the harmonics are compared, a clear difference can be observed.

IV. CONCLUSIONS

The information about the consumption of an individual appliance offers a new perspective on how the energy is used and helps the consumer find solutions in order to reduce and the energy consumption and to improve its management. Considering these, a new algorithm that characterizes the appliances based on their electrical signatures was presented. The parameters which form the signatures are the amplitudes and phases of the current harmonics and the active and reactive powers determined by a consumer switching from one state to another. It was shown that these parameters can be used to differentiate between appliances of similar power or different operating states of the same appliance.

Using the amplitudes and phases of current harmonics up to the 19th order, there can be determined a complex electrical signatures with a large number of monitored parameters which can provide a high degree of granularity for the appliances in a house. In other words, by monitoring a number of 20 parameters one can made a better classification of the appliances than when using a smaller number – 2 for example: active and reactive powers.

ACKNOWLEDGEMENT

This work was supported by a grant of Romanian National Authority for Scientific Research, CNDI-UEFISCDI, project "Smart metering device with incorporated load identification features" SigMET, 30_PCCA_2012.

REFERENCES

[1] K. C. Armel, A. Gupta, G. Shrimali, and A. Albert, "Is disaggregation the holy grail of energy efficiency? The case of electricity", Energy Policy, vol. 52, pp.213-234, 2013.

[2] B. Neenan and J. Robinson, "Residential Electricity use Feedback: A Research Synthesis and Economic Framework", EPRI Technical Update 1016844, Electric Power Research Institute, Palo Alto, CA, 2009.

[3] K. Ehrhardt-Martinez, K. A. Donnelly, and J. A. Laitner, "Advanced Metering Initiatives and Residential Feedback Programs: A Meta-Review for Household Electricity-Saving Opportunities", Technical ReportsE105, American Council for an Energy-Efficient Economy, Washington, DC, 2010.

[4] A. S. Ardeleanu, M. Cretu, and C. Donciu, "Electrical signature – a means of improving the management of electricity consumers," Proceedings of the 7th International Conference on Management of Technological Changes, vol. 2, pp. 553-556, 2011.

[5] Branzila M., Alexandru C., Donciu C., et. al., "Virtual environmental measurement center based on remote instrumentation", Environmental Engineering and Management Journal, vol. 6, issue 6, pp. 517-520, 2007.

[6] Branzila M., Alexandru C., Ciobanu C., et. al., "New DAQB and associated virtual library included in LabVIEW for environmental parameters monitoring", 2008 IEEE International Conference on Virtual Environments, Human-Computer Interfaces and Measurement Systems, pp. 121-124, 2008.

[7] Branzila M., Mariut F., Petrisor D., "Virtual Instrument Developed for Adcon Weather Station", Proceedings of the 2012 International Conference and Exposition on Electrical and Power Engineering, pp. 853-856, 2012.

[8] S. Rahimi, A. D. C. Chan, and R. A. Goubran, "Usage monitoring of electrical devices in a smart home", 33rd Annual International Conference of the IEEE EMBS, pp. 5307–5310, 30 Aug - 3 Sep 2011.

[9] A. S. Ardeleanu and C. Donciu, "Nonintrusive Load Detection Algorithm Based on Variations in Power Consumption", 2012 International Conference and Exposition on Electrical and Power Engineering (EPE), pp. 309-313, 25-27 Oct. 2012.

[10] M. Figueiredo, A. Almeida, and B. Ribeiro, "Home electrical signal disaggregation for non-intrusive load monitoring (NILM) systems", Neurocomputing, vol. 96, pp. 66-73, 2012.

[11] C. Belley, S. Gaboury, B. Bouchard, and A. Bouzouane, "An efficient and inexpensive method for activity recognition within a smart home based on load signatures of appliances", Pervasive and Mobile Computing, vol. 12, pp. 58-78, 2014.

[12] M. Temneanu and A.S. Ardeleanu, "Hardware and software architecture of a smart meter based on electrical signature analysis", 2013 8th International Symposium on Advanced Topisc in Electrical Engineering (ATEE), pp. 1-6, 23-25 May 2013.

[13] M. Temneanu and A. Ardeleanu, "Non-intrusive Hybrid Energy Monitoring System", Advanced Materials Research, vol. 837, pp. 495-499, 2014.

[14] S. Patel, T. Robertson, J. Kientz, M. Reynolds, and G. Abowd, "At the flick of a switch: detecting and classifying unique electrical events on the residential power line", UbiComp 2007: Ubiquitous Computing, pp. 271-288, 2007.

[15] M. S. Tsai and Y. H. Lin, "Modern development of an Adaptive Non-Intrusive Appliance Load Monitoring system in electricity energy conservation", Applied Energy, vol. 96, pp. 55-73, 2012.

[16] S. Gupta, M. S. Reynolds, and S. N. Patel, "ElectriSense: single-point sensing using EMI for electrical event detection and classification in the home", Proceedings of the 12th International Conference on Ubiquitous Computing (Ubicomp 2010), pp. 139-148, 2010.

[17] C. Donciu, A.S. Ardeleanu, and M. Temneanu, "Multi-feature Load Detection Algorithm", Advanced Material Research, vol. 772, pp. 448-454, 2013.

[18] H. H. Chang, C. L. Lin, and J. K. Lee, "Load identification in nonintrusive load monitoring using steady-state and turn-on transient energy algorithms", 2010 14th International Conference on Computer Supported Cooperative Work in Design (CSCWD), pp. 27-32, 2010.

[19] Y. H. Lin and M. S. Tsai, "A novel feature extraction method for the development of nonintrusive load monitoring system basen on BP-ANN", International Symposium on Computer, Communication, Control and Automation, pp. 215-218, 2010.

[20] H. H. Chang, K. L. Chen, Y. P. Tsai, and W. J. Lee, "A new measurement method for power signatures of nonintrusive demand monitoring and load identification", IEEE Transactions on Industry Applications, vol. 48, issue 2, pp. 764-771, 2012.

[21] G.W. Hart, "Nonintrusive appliance load monitoring", Proceedings of the IEEE, vol. 80, pp. 1870-1891, 1992.

[22] A. Cole and A. Albicki, "Nonintrusive identification of electrical loads in a three-phase environment based on harmonic content", Proceedings of the IEEE Conference on Instrumentation and Measurement Technology, pp. 24-29, 2000.

[23] M. Berges, E. Goldman, H. S. Matthews, and L. Soibelman, "Learning systems for electric consumption of buildings", Proceedings of ASCE International Workshop on Computing in Civil Engineering, 2009.

[24] K. D. Lee, S. B. Leeb, L. K. Norford, P. R. Armstrong, J. Holloway, et al., "Estimation of variable-speed-drive power consumption from harmonic content", IEEE Transactions on Energy Conversion, vol. 20, pp. 566-574, 2005.

[25] W. Wichakool, A. T. Avestruz, R. W. Cox, and S. B. Leeb, "Modeling and Estimating Current Harmonics of Variable Electronic Loads", IEEE Transaction on Power Electronics, vol. 24, pp. 2803-2811, 2009.

[26] Branzila M., David V., "Real Time Electrocardiogram Signal Processing for R Peak Detection Using Wigner and Wavelet Functions", Environmental Engineering and Management Journal, vol. 12, issue 6, pp. 1207-1214, 2013.

[27] Branzila M., David V., Padole C., "ECG Signal Processing Using Wigner Function", Proceedings of the 2012 International Conference and Exposition on Electrical and Power Engineering, pp. 601-604, 2012.

[28] S. Giri, M. Bergés, and A. Rowe, "Towards automated appliance recognition using an EMF sensor in NILM platforms", Advanced Engineering Informatics, vol. 27, issue 4, pp. 477-485, 2013.

[29] Y. Kim, T. Schmid, Z. Charbiwala, and M. Srivastava, "ViridiScope: design and implementation of a fine grained power monitoring system for homes", Proceedings of the 11th International Conference on Ubiquitous Computing, pp. 245-254, 2009.

[30] A. S. Ardeleanu and C. Donciu, "Frequency Estimation Based on Variable Frequency Resolution Concept", 2012 International Conference and Exposition on Electrical and Power Engineering (EPE), pp. 792-797, 25-27 Oct. 2012.

[31] C. Donciu and O. Costea, "Intelligent system for precision irrigation of greenhouse vegetables", 6th International Conference on the Management of Technological Changes, pp. 669-672, 2009.

Influence of Knitting Techniques on ESD Performances

Marinel Temneanu[1], Andrei Sebastian Ardeleanu[1]
[1]Faculty of Electrical Engineering
“Gheorghe Asachi” Technical University of Iasi
Iasi, Romania
mtemnean@ee.tuiasi.ro, a.ardeleanu@ee.tuiasi.ro

Asim Egemen Yilmaz[2], Mihai Penciuc[3]
[2]Department of Electrical and Electronics Engineering
Ankara University
Golbasi, Ankara, Turkey
[3]Faculty of Textiles, Leather and Industrial management
“Gheorghe Asachi” Technical University of Iasi
Iasi, Romania

***Abstract*—Electrostatic discharges (ESD) cause significant losses to the electronic industry. To reduce these losses, is essential to develop solutions to protect the electronic devices sensible to ESD. On the manufacturing line ESD garments are used to prevent a discharge from the normal clothing of an operator. In this paper the influence of the knitting techniques on ESD performances is investigated. Nine samples made by different knitting techniques are investigated for their ESD properties. The method used for investigation is charge decay time.**

Keywords-ESD protection; charge decay; knitting structures; core conductive fibers

I. INTRODUCTION

Miniaturization of electrical components gave rise to new possibilities to increase the performances and reduce the sizes of electrical devices, but at the same time increased their vulnerability to disturbances of electrostatic origin [1]. Out of these, the electrostatic discharges (ESD) present the highest danger to failures, costing the electronic industry approximately 45 billion dollars per year [2]. The ESD determines 30 – 50% of the rejected products on the production line [3] and malfunctions which represent approximately 6% of the annual sales.

Given these facts it is important to protect sensitive devices to these discharges by using different protection solutions. Most of the ESD which occurs on the manufacturing line are caused by human operators which build up charge by doing normal activities. For example, approximately 12000 V can be generated only by walking on a polyethylene carpet [4]. When the charge exceeds a certain threshold, which depends on the humidity, surface resistivity or distance to the victim object, a discharge occurs. To prevent this for happening, ESD protective garments, worn over the normal clothing, can be used. Over the years the researchers tested different ESD fabrics using various types of active fibers made from metallic materials such as copper, stainless steel or nickel [5], [6-8]. Out of these, the fabrics made with copper fibers were found to have good ESD properties [7]. Lately, besides the fibers from metallic materials, the attention was directed towards the fibers made from carbon [5], [8-11], which also presents good ESD properties.

To assess the performance of the ESD structures, different methods were used to analyze the properties of ESD fabrics. One of the most used methods is surface resistivity measurement, which consists in placing two electrodes at certain distances on the tested fabric and measuring the resistivity between them [5], [7], [11], [12-13]. This method shows the ability of a fabric to quickly dissipate the charge. As stated before, fabrics with dissipative properties are searched. The electric fields generated on the normal clothes could charge, by induction, a nearby object, making it susceptible to electrostatic discharges. Measuring the ability of an ESD fabric to screen those fields can also be used as an investigation method [10], [14]. Given their shielding properties, the ESD fabrics can also be used as electromagnetic shields [15].The method will show the ability of an ESD fabric to reduce the influence of the electric fields generated on the normal clothes. Another method used to assess the performances of ESD fabrics is to analyze the charge decay times [5], [7], [11], which consists in charging the fabrics up to a certain level after which the time needed for the charge to decrease to a certain level is measured.

Within this paper a number of fabrics obtained by different knitting techniques will be investigated for their ESD properties. Therefore the influence of the knitting technique on the performances of the ESD fabrics will be investigated. The investigation will consist in analyzing the charge decay times for the samples charged up to ± 5 kV and ± 3 kV.

II. MATERIALS AND METHODS

The evaluation of the ESD properties was made on 9 samples made by 9 different knitting techniques (Table 1). The knitted structures contain normal loops, retained loops and double loops. The samples were made using a manual knitting machine, fineness 5E, which doesn’t break the thread. The metallic wire (active fiber), a 0.15 mm enameled copper wire, was fed in parallel with acrylic fibers, Nm 32/2/2. The presence of the metallic wire significantly decreases the intensity and duration of relaxation. The enamel will provide a high resistivity interface which will limit the energy transfer in case of an accidental discharge while the copper wire will provide a fast dissipation path of the accumulated charge.

978-1-4799-5849-8/14/$31.00 ©2014 IEEE

TABLE I. PARAMETERS OF KNITTED SAMPLES

Sample code	**Knitting structure**	**Wale density (wale/5cm)**	**Course density (course/5cm)**	**Specific mass (g/m^2)**
PRV	Patent with variable ratio	15.5	13	541
GR	Plating with retained loops	25.5	15	530
P3	Patent 3×3	22.5	16.5	722
P1×1	Patent 1×1	20	12	662
G	Plating	20	16.5	459
MR	Milano Rib	28	12	645
SF	Semifang	11	10.5	672
T	Plating tubular	17	12.5	697
V1R	Wave 1 course	11	12	738

The PRV sample is a modular one, obtained by alternating plating areas with patent areas. The plating with retained loops (GR sample) implies that a loop is not discharged in the cycle immediately following its formation, which leads to its elongation. The P3 sample is characterized by the presence of plating and patent loops, which changes the layout of the wales in relation with the specific layout of the patent 1×1 structure. For the P1×1 sample, the loops are arranged in two planes, corresponding to the two working fronts. The wales with the same aspect tend to become tangent, although the presence of the metallic wire reduces this phenomenon. Sample G is the simplest knitted structure, where the loops are arranged in one plane. The Milano Rib knit one patent course is followed by a tubular plating course. Each wale contains a normal loop and a retained loop. The Semifang knit is a patent 1×1 structure with double loops disposed on only one side. The T sample is characterized by two layers of plating loops, arranged independently (without connecting them). The V1R sample is obtained by knitting a patent course followed by a plating course. Thus, retained loops appear on one side of the knit while normal loops appear on the other side.

The ESD properties of the samples are evaluated using the charge decay method presented in [5]. The measuring stand is composed of a charge plate monitor (CPM), a discharge electrode, a discharge switch and an oscilloscope. The CPM has a power source to charge the samples up to the predefined levels and an electrostatic field meter used to measure the charge. The discharge electrode is designed to allow the connection to the discharge path of one side or both sides of the tested fabric. The discharge switch is used to start the discharging process. The oscilloscope is connected to the CPM's output (electrostatic field meter) and will record the discharge signal. For each sample a number of four charge levels were tested, namely ± 5 kV and ± 3 kV. These measurements were made to investigate how the charge polarity influences the discharge process and how the samples dissipate the charge of different levels.

For each charge level, two measurements were carried out by changing the connection between the sample and the discharge electrode. Thus, one type of measurement was made using a strip of one end of the fabric in contact with the discharge electrode (fabric connection), while the other one was made using only the metallic wire in contact with the discharge electrode (wire connection). This way is analyzed how the direct connection to the ground of the active fiber influences the discharge process. The discharge signals were evaluated by comparison with two thresholds representing the half value ($U/2$) and $1/e$ value (U/e) of the charge level.

III. RESULTS AND DISCUSSIONS

As stated before, 8 measurements of the charge decay times were performed for each of the 9 samples. In the following graphics, the results of these measurements are presented. In Fig. 1, the results obtained when the samples were charged up to 5 kV and the connection between the discharge electrode and the sample was made through a strip of the fabric are presented. In Fig. 1a the discharge signals for the 9 samples are compared with the two thresholds, while in Fig. 1b a column chart with the times needed to reach the U/e value is presented. For the samples that don't reach this value, namely P1×1, G, SF, T, V1R and PRV, the values of the discharge times were set to a maximum value of 0.12 ms. As it can be observed, the samples MR, GR and P3 offer the best charge decay times.

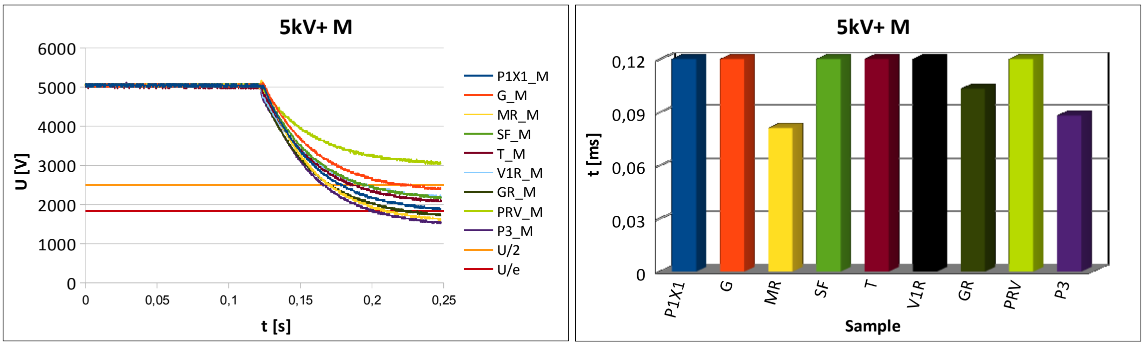

a. b.

Figure 1. Discharge signals (a) and corresponding charge decay times (b) for 5 kV charge, fabric connection

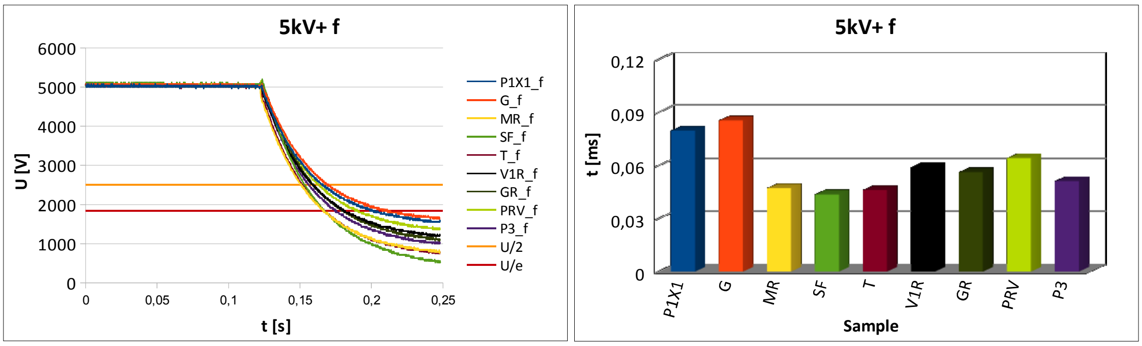

a. b.

Figure 2. Discharge signals (a) and corresponding charge decay times (b) for 5 kV, wire connection

In Fig. 2, the results obtained for the same charge but with the metallic wire connected to the discharge electrode are presented. Comparing these results with the ones presented in the previous figure, an improvement can be seen for all the samples in that all are able to decrease the charge under *U/e* threshold. This improvement is achieved given the reason that a direct connection is made between the discharge electrode and the conductive wire, thus providing a low resistivity path for the charge to dissipate. From these results, MR, SF, T, P3, GR and V1R present the best results.

The results obtained for a negative charge of 5 kV are presented in Fig. 3 and Fig. 4. In Fig. 3 the results obtained for the fabric connection are presented, while in Fig. 4 the results obtained for the wire connection are presented. It can be observed that most of the samples significantly improved their performances while the others slightly decreased their results. Overall the samples presented better results for the negative charge than for the positive charge. As with the positive charge better results can be observed for the wire connection than for the fabric connection. The best results are achieved by samples P1×1, G, MR, T and PRV for fabric connection and samples P1×1, G, MR, T and V1R for wire connection.

For a 3 kV charge the results obtained for the fabric connection are presented in Fig. 5 while for the wire connection in Fig. 6. Again, better results are obtained when the copper wire is connected to the discharge electrode. From the fabric connection the sample G stands out while from the wire connection samples P1×1, G, MR, SF and V1R present the best results. The results for the negative 3 kV charge are presented in Fig. 7 and Fig. 8 from which, as in the 5 kV case, an overall improvement can be observed when compared with the positive charge. The samples that present the best results are P1×1, G, MR and GR for the fabric connection and P1×1, G, MR, T, V1R, GR and P3 for the wire connection.

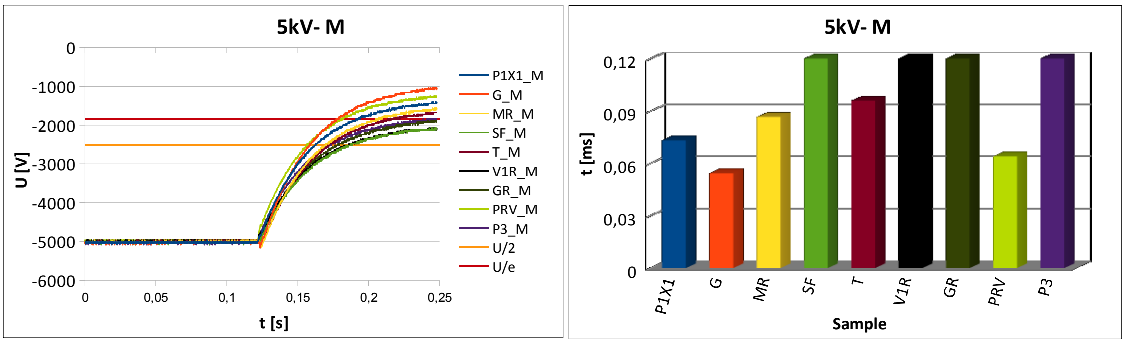

a. b.

Figure 3. Discharge signals (a) and corresponding charge decay times (b) for -5 kV charge and fabric connection

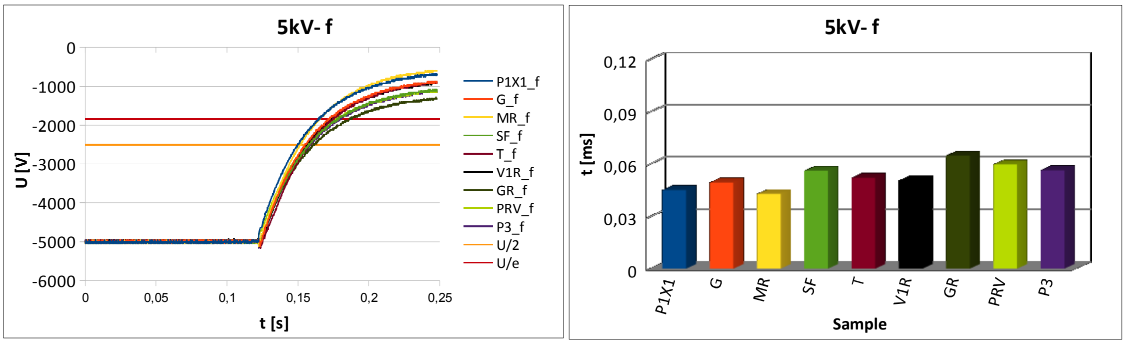

a. b.

Figure 4. Discharge signals (a) and corresponding charge decay times (b) for -5 kV charge and connection though the metallic wire

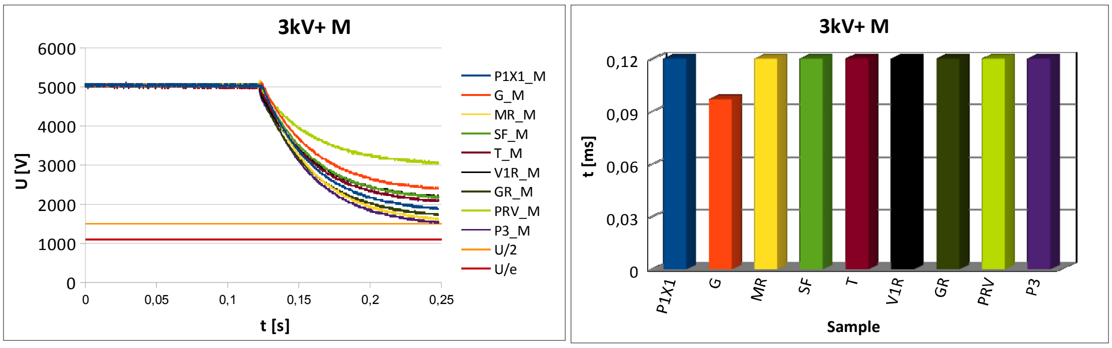

a. b.

Figure 5. Discharge signals (a) and corresponding charge decay times (b) for 3 kV charge and fabric connection

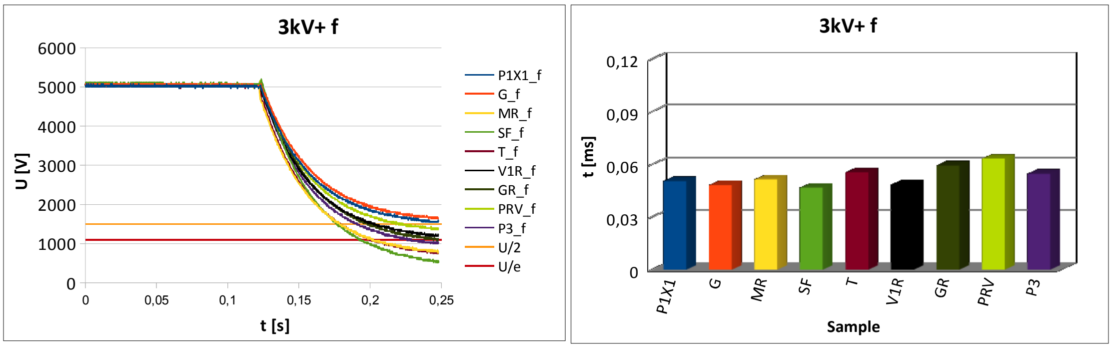

a. b.

Figure 6. Discharge signals (a) and corresponding charge decay times (b) for 3 kV charge and wire connection

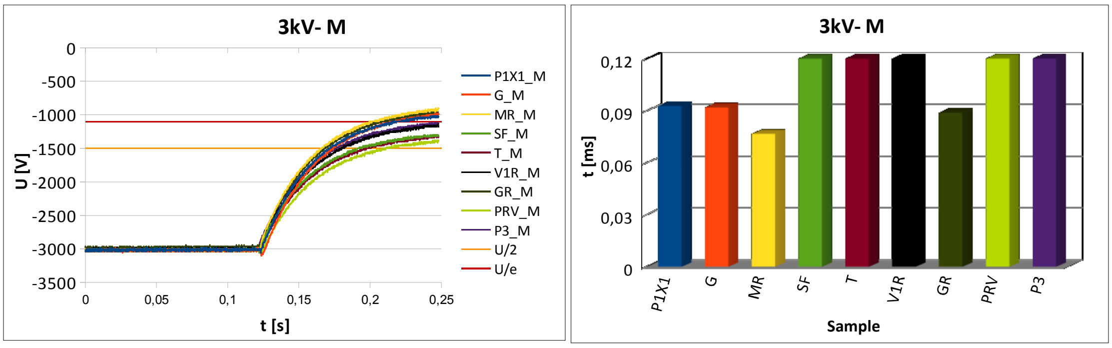

a. b.

Figure 7. Discharge signals (a) and corresponding charge decay times (b) for -3 kV charge, fabric connection

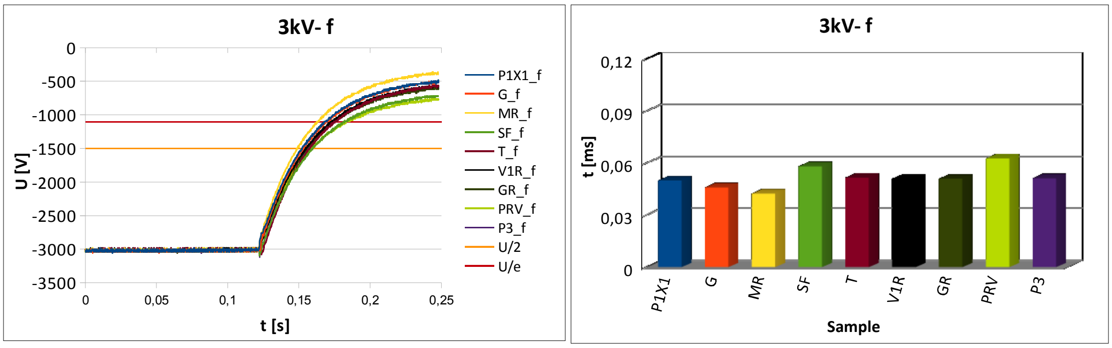

a. b.

Figure 8. Discharge signals (a) and corresponding charge decay times (b) for -3 kV charge, wire connection

IV. CONCLUSIONS

Using wires with conductive core allows for two important characteristics to be obtained, namely:

- Providing dielectric properties to the external layer of the knitted samples that do not facilitate the migration (discharge) of the accumulated charge;
- Providing a discharge path for the accumulated charge, through their conductive core.

According to the experimental results, a direct connection between the active wire and the discharge electrode ensures the samples a better ability to dissipate the charge than when a strip of the fabric is connected to the discharge electrode. This is due to a lower contact resistance between the electrode and the charge path. Comparing the samples' behavior, in terms of ESD performance, when they were charged either positive or negative, an overall better dissipation of charge was observed for the negative charge. The tests relating to the ability of charge dissipation revealed that the knitting techniques used to make the samples MR, G and P1×1 as the best to be used in developing ESD protective structures.

ACKNOWLEDGMENT

This work was jointly supported by grants of the Romanian National Authority for Scientific Research, CNDI–UEFISCDI (with CrossTexNet Project ID 7_071_2012) and the Scientific and Technological Research Council of Turkey, TÜBİTAK (with Project ID 9110018). The authors would like to express their gratitude to these institutions for their support.

REFERENCES

[1] J. Paasi, "Assessment of ESD threats to electronic components", Journal of Electrostatics, vol. 63, issues 6–10, pp. 589-596, 2005.

[2] K. Allen, "How ESD damage affects OEMs and what they can do to mitigate the damage", PC/104 Embedded Solution, 2002.

[3] J. Paasi, S. Nurmi, T. Kalliohaka, G. Coletti, F. Gustavino, et al., "Electrostatic testing of ESD protective clothing for electronics industry", Electrostatics 2003 Conference, pp. 239–246, 2003.

[4] K. B. Cheng, T. H. Ueng, and G. Dixon, "Electrostatic discharge properties of stainless steel/polyester woven fabrics", Textile Research Journal, vol. 71, pp. 732–738, 2001.

[5] C. Donciu, "ESD garments with bilayer structure", Advanced Materials Research, vol. 837, pp. 682–687, 2014.

[6] H. S. Chen, K. C. Lee, and J. H. Lin, "Electromagnetic and electrostatic shielding properties of coweaving-knitting fabrics reinforced composites", Composites Part A-Applied Science and Manufacturing, vol. 35, issue 11, pp. 1249–1256, 2004.

[7] C. Donciu, "Core Conductive yarn based integral knitted ESD garments Part I. Metallic core conductive yarns investigation", Advanced Materials Research, vol. 772, pp. 467–473, 2013.

[8] C. Donciu, "Estimating ESD properties of fabrics based on correlation between dielectric losses and charge decay time", Advanced Materials Research, vol. 837, pp. 688–693, 2014.

[9] M. Cieslak, S. Wrobel, I. Kaminska, and M. Lao, "Functional upholstery materials for protection against electrostatic risk", Fibres and Textiles in Eastern Europe, vol. 17, pp. 52–58, 2009.

[10] L. Fast, A. Börjesson, and J. Paasi, "Can ESD-protective garments screen static electric fields?", Journal of Electrostatics, vol. 63, issue 6-10, pp. 621–626, 2005.

[11] C. Donciu, "Core conductive yarn based integral knitted ESD garments Part II. Carbon composite yarns investigation", Advanced Materials Research, vol. 772, pp. 474–479, 2013.

[12] Standard EN 1149-1: Protective clothing – Electrostatic properties – Part 1: Test methods for measurement of surface resistivity, 1996.

[13] Standard IEC 61340-5-1: Protection of electronic devices from electrostatic phenomena – General requirements, 1998.

[14] J. N. Chubb, "Tribocharging studies on inhabited cleanroom garments", Journal of Electrostatatics, vol. 66, pp. 531–537, 2008.

[15] C. Donciu, "3D conductive textile shields", Advanced Material Research, vol. 837, pp. 340–345, 2014.

THE 8th INTERNATIONAL SYMPOSIUM ON ADVANCED TOPICS IN ELECTRICAL ENGINEERING
May 23-25, 2013
Bucharest, Romania

Hardware and Software Architecture of a Smart Meter Based on Electrical Signature Analysis

Marinel Temneanu, Andrei Sebastian Ardeleanu
“Gheorghe Asachi” Technical University of Iasi, Faculty of Electrical Engineering, 21-23 Profesor Dimitrie Mangeron Blvd, 700050, Iasi, Romania,
mtemnean@ee.tuiasi.ro, a.ardeleanu@ee.tuiasi.ro

***Abstract*-The main resources used in electricity generation are becoming fewer, while the impact of renewable resources is still quite small. To allow the necessary time for the technology of renewable resources to mature, a requirement is to increase the energy efficiency. In this regard the smart grid concept was implemented, but whose efficiency depends on creation of a framework through which the end user can actively participate in the energy marketplace. End users must be able to understand how the energy is used so that they could find possibilities to increase the efficiency of energy. Within this paper the architecture of a smart system (smart meter) capable to disaggregate the whole energy consumption into individual consumers is presented. This way, the user will have a better understanding on how the energy is used, will find major consumers and will be able to reduce his consumption.**

***Keywords*: smart meter, nonintrusive load monitoring, energy disaggregation.**

I. INTRODUCTION

Electricity has become an indispensable good of the current time as it’s used to power the majority of devices commonly used every day. Since its commercial use, one of the most important concerns was monitoring the electricity consumption. This was due to a certain number of reasons, such as: power quality monitoring, obtain estimates regarding the energy use or determine possibilities to reduce energy consumption [1]. Nowadays, when resources are getting increasingly scarce it’s important to improve the management of both energy generation and consumption [2]. European Union decided to reduce the level of greenhouse gasses by 20%, to increase the penetration of renewable energy resources by 20% and to increase the energy efficiency by 20% by year 2020 [3]. Most of the current research was directed to increase energy efficiency of electrical devices, but this efficiency also depends on the choices the consumers make. Using time differentiated tariffs and economic incentives, utility providers have tried to determine users to shift usage to off-peak hours. With the classical electricity meters this is hard to achieve, since the information regarding the consumption is given in an abstract and unfamiliar form of the entire consumption for a specified period of time. To overcome this issue, a new type of meters was implemented, the so-called smart meters, which present the consumption in a more efficient way, in form of real-time graphs.

To increase the awareness on how the energy is consumed, smart meters can be equipped with disaggregation functions which allow them to present the consumption of each individual appliance within a house. This way, the user will have a better understanding on how the energy is used, where the inefficiencies come from and will be able to identify possibilities to improve the efficiency of energy consumption [1]. Consumption disaggregation techniques can be classified in intrusive and nonintrusive load monitoring techniques. The first one uses a network of meters, connected to each individual consumer, which send the consumption information to a central display device. The second technique uses a single meter that analyses the variations of voltage and current to determine certain events that relate with the transition of a consumer from one state to another. This technique has the advantages of a simple architecture and low cost but it requires complex software to identify the characteristics needed to detect a consumer. These characteristics represent the electrical signature and define the electrical behaviour of an individual appliance when it is operating.

The idea of nonintrusive load monitoring belongs to G.W. Hart who observed that he can see what happens within a house, in terms of appliance using, by simply analysing the variations in power consumption [4]. The algorithm identifies the consumers as finite state machines, where transitions from one state to another represent the change in the operating status. To better track variations over time, an algorithm that segments the power based on variations in current’s RMS values was implemented [5].

Consumers with similar steady-state variations can generate different transient signals, when switching from one state to another. The shape of these signals depends on the physical task to be performed and can be used to detect the consumers [6-9]. These signals can be distinguished by analysing their particularities, such as: duration, amplitude, time constant, etc.

Analysis of spectral components can also be used to characterize the consumers’ electrical signature [10-15]. Non-linear loads, unlike the linear loads, don’t draw only currents of fundamental frequency but also currents of harmonic frequencies. Using different frequency estimation techniques [16-18] the spectral content can also be used to detect the presence of a consumer in total load. Different researchers have found that there are correspondences between the fundamental and different harmonic components [11, 15]. Using these correspondences, variable consumers can be detected and extracted from the total load.

978-1-4673-5980-1/13/$31.00 ©2013 IEEE

A combination of different characteristics such as instantaneous admittance, instantaneous power, current waveform and eigenvalues was used as features to characterize the electric load signature [19-20]. Depending on the electrical structure the current waveform has different shapes from one consumer to another. Also because devices have different current consumptions the instantaneous admittance and instantaneous power can offer information about the operating status of a device. The dynamics of variable loads can be observed by applying the eigenvalue analysis of the time series of the current waveform rearranged into a matrix form.

A different approach to detect the presence of a consumer consisted in analysing the noises that occur in the electrical network [21]. It was noticed that when a consumer switches from one state to another it generates a transient signal (noise) whose spectral analysis can be used to define the consumer's electrical signature. Permanent noises (waveform distortions) were also observed during the operating state of a consumer, which can be used to detect the presence of a consumer.

In this context, the current paper describes the hardware and software architectures of a smart meter, SigMET, capable to distinguish energy consumption for each consumer. Classifying individual consumption will be achieved by a method of analysis and interpretation of different electrical characteristics. Thus, using only a single general meter, differentiation between consumers will be made based on the electrical signature. Smart meter's operation will include a calibration procedure in its installation or during its operation, when introducing a new consumer. This procedure aims to detect the consumer's electrical signature which will be stored into the smart meter's memory and further used in consumers' detection.

II. SMART METER'S ARCHITECTURE

SigMET's general architecture, which will be described in the current paper, is presented in Fig. 1. For this architecture was opted for a single data acquisition and transmission module (DAM) which has the role to transmit the measurements regarding the global consumption. Data processing for electrical energy calculation along with disaggregation of total consumption into individual consumers is achieved by the electrical signature identification algorithm (ESI) existent on the data processing module (DPM).

Basic functionalities accomplished by SigMET are: measuring the required electrical measures, data processing (measurement of global electrical energy consumption and disaggregation of total load into individual consumers), data store (data regarding the global/individual consumptions, electrical signatures database of the detected consumers and access/identification data), data communication between the modules or system's subcomponents and data display.

A. *Sigmet's Hardware Architecture*

Block Diagram of Hardware System

Structurally, SigMET's hardware architecture's is composed of two main modules, DAM and DPM, each interacting with each other but also with external factors (Fig. 2).

DAM's main function is represented by the acquisition of the electrical measures of interest, while DPM's main function is to process the acquired data. Each module consists of several blocks that help in achieving the main function and other auxiliary blocks needed for the whole system to operate.

DAM blocks involved in providing the main function are:

- Signal conditioning: transforms the voltage and current levels to values compatible with the multiplexor's input;
- Multiplexor: successively connects the two channels to digital-analogue converter's input;
- Digital-analogue converter (DAC): samples, quantifies and encodes the continuous time variable voltage segments.

The blocks supporting the main function and/or have an auxiliary role are: memory, microprocessor, wireless and power line communication (PLC) and power supply.

DPM blocks involved in providing the main function are:

- Central processing unit: controls the rest of hardware devices, transmits task to each hardware component, coordinates and verifies the execution of the tasks;
- Volatile memory: space where SigMET's software applications are executed;
- Non-volatile memory: SigMET's software architecture residence.

The blocks supporting the main function and/or have an auxiliary role are: display, wireless communication, PLC communication, Ethernet communication and power supply.

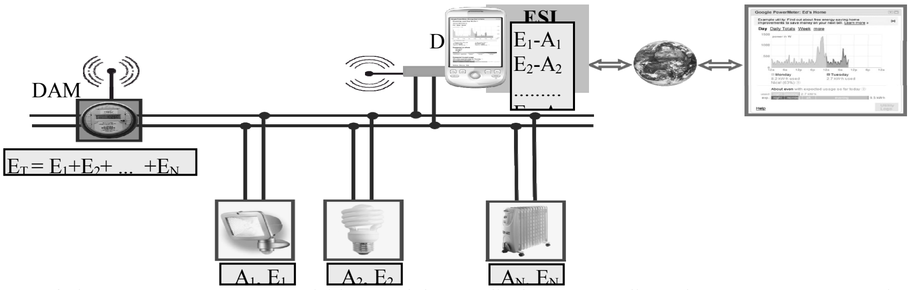

Fig. 1. General architecture of SigMET: DAM – Data Acquisition Module, D – display, A_i – appliance i, E_i – energy consumption for A_i, ESI – Electrical Signature Identification.

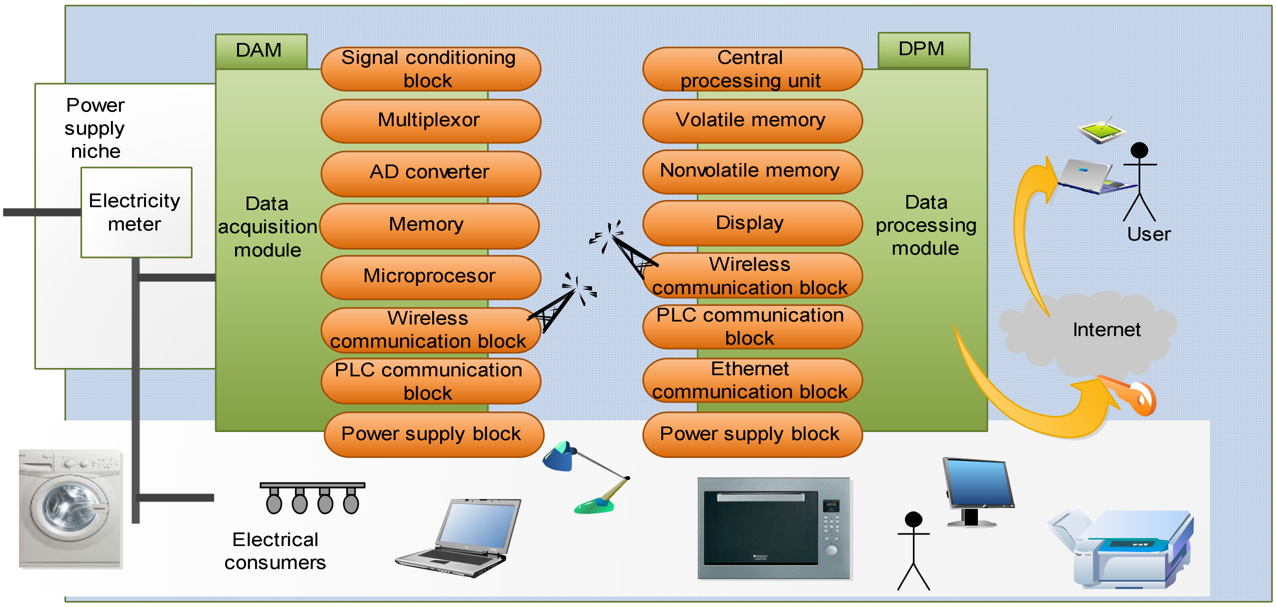

Fig. 2. SigMET's hardware architecture.

Operation of Hardware System

DAM is mounted in the vicinity of power supply niche to have access to the global voltage and current within the house. These parameters are measured with the signal conditioning block mounted on a rigid structure with protection against unauthorized access. Acquired data of voltage and current are transmitted, after having first been converted to digital code, to DPM. Data transmission can be made through power line communication [22-23] or radio.

At DPM level the acquired samples are numerically processed and the results are sent to the user. The information can be provided locally through the display or remotely through the internet page generated by DPM.

B. Sigmet's Software Architecture

Block Diagram of Software System

SigMET's software can be seen as a system composed of multiple subsystems, each interacting with a number of other participants. The following describes the two main subsystems:

a) SigMET Server runs the DPM and is responsible for the following tasks:

- Acquisition of current and voltage waveforms from the power supply niche (data acquisition module);
- Electrical signature identification (ESI) for each consumer that contributes to the total consumption and estimation of the energy consumed by each consumer (ESI module);
- System configuration: define the consumers, work parameters, configure learning and working phases;
- Database responsible for storing and maintaining the data;
- Data server: receives the information about the electrical power of each consumer and stores it in the database, processes the data and makes reports;
- Web page: is an Web server that can be accessed on any internet browser to display the reports;
- TCP/IP comunications: is the module through which SigMET Server communicates with SigMET Client to transmit the measurement data and the reports;

b) SigMET Client is an application that runs on a mobile phone or a tablet with touch screen, through which the user has the possibility to visualize the data regarding the electricity consumption and transmit work commands to the server. It consists of the following blocks:

- TCP/IP communication module through which the client application communicates with the data server;
- Display module – responsible with the graphic display of the information to the user;
- User input: records the user commands and send them to the system;
- Data storage: allows the client application to store and access the work data;
- Data processing: processes the data to obtain the complex measurement information;
- SigMET Controller: central module that provides the communication between all application modules and is used to implement the Model View Controller (MVC) architecture.
- The participants with whom SigMET interacts are:
- End user: the user who will have the SigMET installed and which will benefit of the measurement data. For this participant, different Use Cases (UC) are attributed, by which the user interacts with the system to configure or change the work procedure.
- Internet and Wi-Fi: the participant through which the system connects to the internet network.
- Power supply niche: the point where the system collects the current and voltage data and consists of the electrical power supply wires of the building.

- Time: the participant that synchronizes the system and is used in measuring and periodic transmission of the energy consumptions.

C. Service Orientated Architecture (SOA)

For SigMET's software component a service-oriented architecture is used, where the services are code segments that perform certain tasks and can be reused within the system to resolve different tasks. SOA isn't an actual API (Application Programming Interface), but it rather defines the interface between the software components, based on protocols and functionality. Within SOA there are suppliers and consumers. The services will communicate with each other through a well defined dataset, visible throughout the application.

The advantage of this architecture is that services aren't connected with each other and can be developed and tested independently of each other. This allows the teams of programmers to work in parallel, test their services and after that to integrate them into the final system.

In SigMET system, each subsystem can be seen as a set of services associated with an UC. The services will be implemented separately, tested using specific test cases (TC) and integrated in the final application. For SigMET Server the following services are attributed: waveform acquisition, consumer's electrical signature identification, database storage, data processing and reporting, TCP/IP data transmission, Web page display and system configuration. For SigMET Client the following services are attributed: data display, TCP/IP data transmission, data processing and store and system setup.

D. Architecture of Electrical Signature Identification System

Electrical signature can be defined as a set of electrical parameters which can be used to detect the operating status of an electrical consumer at a time. The parameters that can characterize the electrical signature are: active and reactive power changes, current's harmonics, instantaneous power, admittance, phase shift between voltage and current or current's waveform.

Using the sensorial part of the SigMET the current and voltage are measured and conditioned to compatible levels. Using these signals the algorithm proceeds to the next stage, the event detection. An event can be defined as a consistent change of the parameters of interest, which can be determined by the transition of a consumer from one state to another. Detection of these changes is made based on predefined thresholds, whose values must be high enough to not detect false events, but also low enough to detect the smaller consumers. Transient events that aren't caused by switching a consumer will be eliminated.

The parameters used to define the electrical signature will be determined only if an event is detected. This avoids loading the algorithm with a set of operations that are not necessary when no consumers are switched. The parameters which can be used are: phase shift between current and voltage, active and reactive power changes or current's harmonics.

Depending on the consumer's electrical structure the phase shift between the current and voltage can take different values. For resistive consumers the phase shift is 90º while for other types of consumers, depending on the inductive or capacitive components used, the phase shift will take different values that can be used in consumers' detection.

A consumer's switch is accompanied by different changes in the energy consumption. These changes are different from one consumer to another, and so may be used in consumer detection. It is therefore useful to calculate the active and reactive powers. Both powers are used as may be consumers who determine similar changes of one power but totally different of the other one.

Depending on their electrical components, the consumers can draw currents both at fundamental frequency and at higher harmonic frequencies. Spectral content can differ from one consumer to another, thus it is also useful to determine the harmonic components of the drawn current. A study on different consumer categories is required, to determine the highest harmonic that can cause substantial changes. Through this study the algorithm will be optimized so that it will determine only the part of interest from the spectral spectrum.

It's important that measured parameters follow as closely as possible the variations that occur when a consumer switches from one state to another. Of the two measured signals, the current is the one that varies when a consumer is switched. Taking this into account, the algorithm must be implemented so that the analyzed parameters are calculated when consistent changes of the current occur.

Detected events can be analyzed both in steady state and transient regime. Therefore, an event will be characterized by the changes of the analyzed parameters and their transient profile recorded when a consumer switches from one state to another. Taking into account that transient signals can vary from milliseconds to seconds, the algorithms must be implemented so they can adapt to these variations. For example, transient signals for resistive consumers may be missing or have a very short duration, while pump operated devices can have long transient signals. The algorithm must take into account this fact; it must be able to analyze the data at high frequencies for long periods of time.

Based on detected events, the algorithm will proceed with the electrical signature identification which corresponds with consumers' detection. For this, a database that contains the consumers' electrical signatures is required. This database can be made at the beginning during a learning stage or on the way while different electrical signatures are detected. The first version presents the following advantages:

- Detected electrical signatures will take average values of a consumer operating status, thus reducing the risk for an electrical signature to belong to a particular case;
- An equivalence between an electrical signature and a consumer can be made (consumers' naming can be made);
- Multi-state consumers can be identified correctly, avoiding situations where states of these consumers can be assigned to different consumers.

This version presents and disadvantages:

- The implemented algorithm is not autonomous – depends of this learning stage that will be done by a qualified operator;
- Problems can occur when consumers that weren't previously defined are detected.

The second version presents the following advantages:

- The implemented algorithm is autonomous, won't require the intervention of qualified personnel;
- It can adapt to different environments, it doesn't require a previously configuration.

This also presents disadvantages:

- There is the possibility that a multi-state consumer determine detection of other consumers with similar parameter changes;
- Initial detection of a consumer may correspond to a particular situation, so that future switches of the same consumer determine detection of different consumers;
- Difficulties regarding the consumers' naming.

Within the second version the initial consumers' detection can be made based on the principle that the sum of all power changes, determined by an electrical consumer during an off-on-off cycle, is zero or close to zero. Using the database generated through the consumers' input interface, the algorithm will proceed with the consumers' detection. This consists in searching in the database consumers who have the same parameters with the electrical signature of the current detected event.

In practice there may be situations where two or more consumers are switched at the same time. For this purpose, a routine that takes into account these situations will be implemented. When for a transition no consumer is identified, this routine will generate combinations of consumers to determine if that transition can be determined by the simultaneous switch of several consumers.

A routine will also be implemented that will take into account the values of the parameters when no consumer is turned on. When this level is achieved, the operating states of all detected consumers are analyzed. If a consumer is found to be turned on then automatically it will be switched to off state. The transitions that determined the on state for the consumers found as turned on will be reviewed in order to determine if they could have been caused by a new consumer.

As consumers are identified, the overall consumption is broken down into consumptions for each individual consumer. These values are recorded into a database and will be used for statistical reports. Also this information will be provided to the user through a graphic interface.

III. EXPERIMENTAL DATA

The following experimental data will present the principle of consumers' detection based on their electrical signature. The parameters which will be analysed to determine the electrical signatures are the variations in time of active and reactive powers. In Fig. 3 is presented the evolution of active and reactive powers when 4 different consumers are switched from one state to another. Data shown are obtained after a previously segmentation was performed to separate the steady states from the transient states. For a better analysis of the experimental data and a better understanding how the consumers' detection is achieved, active and reactive power changes (ΔP and ΔQ) are presented in Table 1. Since no consumer was previously detected, new consumers will be detected and their electrical signature will be stored in the database. The second version of database generation is chosen because it's autonomous and doesn't require any external intervention. As stated before, the initial consumers' detection is made on the principle that the sum of all power changes, determined by a consumer during an off-on-off cycle, is zero or close to zero. The parameters of transient profiles that have not been assigned to any device are recorded into the $\boldsymbol{\Delta P}$ and $\boldsymbol{\Delta Q}$ vectors. As new transient profiles are detected the corresponding power changes are compared with different combinations made with the items of $\boldsymbol{\Delta P}$ and $\boldsymbol{\Delta Q}$ vectors. Since the values of the power changes are affected by measurement and calculation errors, thresholds are taken into consideration when the comparison is performed: $\Delta P_{thr+} = |\Delta P| \times 110\% + l_{fa}$, $\Delta P_{thr-} = |\Delta P| \times 90\% - l_{fa}$, $\Delta Q_{thr+} = |\Delta Q| \times 110\% + l_{fr}$, $\Delta Q_{thr-} = |\Delta Q| \times 90\% - l_{fr}$, where l_{fa} and l_{fr} are fixed additional limits for the active and reactive power changes. These limits are added to take into account the variations that occur on small power changes and determine a percentage variation larger than 10%. For example an incandescent bulb determines a small reactive power change of the order of a few VAR's. If one time determines a power change of 1 VAR and another time a power change of 2 VAR, is obvious that the 10% limit isn't enough. Thus, the two additional limits are used, and their values are chosen to 1 W for l_{fa} and 5 VAR for l_{fr}. The higher value for l_{fr} was chosen, since from the experimental research, higher variations were observed in the case of the reactive power changes.

From Table 1 it can be seen that, until the seventh state (t = 126 s) no consumer is detected, since no combination of power changes is found within the predefined limits. For the 7th state the following limits are calculated: $\Delta P_{prag-} = |-22.51| \times 90\% = 20.26$ W, $\Delta P_{prag+} = |-22.51| \times 110\% = 24.76$ W, $\Delta Q_{prag-} = |-23.63| \times 90\% - 5 = 16.27$ VAR, $\Delta Q_{prag+} = |-23.63| \times 110\% + 5 = 30.99$ VAR. Each of the undefined vectors contains 5 elements, which can be used to generate 31 combinations. Among them, only one falls within the limits: 20.44 W and 22.13 VAR corresponding to the 5th state. Since no consumer is registered in the database, it is considered that a new consumer was detected, whose information will be recorded in the database.

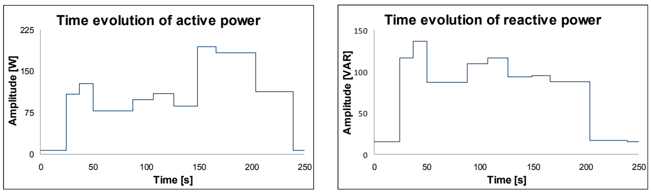

a. b.

Figure 3. Evolution of powers generated by switching on and off 4 consumers: a. active power evolution; b. reactive power evolution.

TABLE I
EVOLUTION OF POWER CHANGES AND CONSUMER DETECTION PROCESS

No.	t_{start} ^{a} [s]	ΔP [W]	ΔQ [VAR]	$\boldsymbol{\Delta P}$ [W]	$\boldsymbol{\Delta Q}$ [VAR]	Detected consumer [W, VAR]
1.	0	7.14	15.33	[ ]	[ ]	-
2.	24	101.48	100.91	[101.48]	[100.91]	-
3.	37	18.65	20.45	[101.48, 18.65]	[100.91, 20.45]	-
4.	50	-49.75	-49.68	[101.48, 18.65, -49.75]	[100.91, 20.45, -49.68]	-
5.	88	20.44	22.13	[101.48, 18.65, -49.75, 20.44]	[100.91, 20.45, -49.68, 22.13]	-
6.	107	10.22	7.17	[101.48, 18.65, -49.75, 20.44, 10.22]	[100.91, 20.45, -49.68, 22.13, 7.17]	-
7.	126	-22.51	-23.63	[101.48, 18.65, -49.75, 10.22]	[100.91, 20.45, -49.68, 7.17]	[21.48, 22.88]
8.	149	106.69	0.98	[101.48, 18.65, -49.75, 10.22, 106.69]	[100.91, 20.45, -49.68, 7.17, 0.98]	-
9.	166	-10.89	-8.14	[101.48, 18.65, -49.75, 106.69]	[100.91, 20.45, -49.68, 0.98]	[10.55, 7.65]
10.	204	-70.24	-71.10	[106.69]	[0.98]	[120.13, 121.35]
11.	240	-106.48	-1.32	[ ]	[ ]	[106.58, 1.15]

^{a}Start time of the current power change

The algorithm continues similarly to analyse all the states, and thus other 3 new consumers are detected, as it can be seen in "Detected consumer" column from Table 3.1.

IV. CONCLUSIONS

In this paper the architecture of a smart meter was presented. Unlike a classic electricity meter the smart meter offers a more detailed package of information about the electricity consumption. The information is offered in real-time in a more familiar way, in form of graphs, not as abstract as in the case of the classic meter that offers a single value about the whole consumption at a time. Also the information about the consumption is disaggregated into individual consumers, which offers the user a clearer view about how the energy is used. The user will have a better understanding about his energy use, will know which are the major consumers, how and when they consume energy. This gives the user the ability to find possibilities to improve his energy use which will lead to a reduction in his carbon footprint and also in consumption of resources used in electricity generation.

ACKNOWLEDGMENT

This work was supported by a grant of the Romanian National Authority for Scientific Research, CNDI–UEFISCDI, project "Contor inteligent bazat pe evaluarea semnaturii energetice" SigMET, 30_PCCA_2012.

REFERENCES

[1] T. Ueno, R. Inada,O. Saeki, and K. Tsuji, "Effectiveness of displaying energy consumption data in residential houses. Analysis of how the residents respond," *ECEEE 2005 Summer Study Proc.*, vol. 3, pp. 1289-1301, 2005.

[2] A.S. Ardeleanu, M. Cretu, and C. Donciu, "Electrical signature – a means of improving the management of electricity consumers," *Proc. of the 7th Int. Conf. on Manag. of Technol. Changes*, vol. 2, pp. 553-556, 2011.

[3] World Business Council for Sustainable Development, "Energy efficiency in buildings: Business realities and opportunities," Technical report, 2008.

[4] G.W. Hart, "Nonintrusive appliance load monitoring," *Proc. of the IEEE*, vol. 80, pp. 1870-1891, 1992.

[5] A.S. Ardeleanu, C. Donciu, "Nonintrusive load detection algorithm based on variations in power consumption," *Proc. of the 2012 Int. Conf. and Exp. on Electrical and Pow. Eng.*, pp. 792-797, 2012.

[6] S.B. Leeb, and J.L. Kirtley, "A multiscale transient event detector for nonintrusive load monitoring," *Proceedings of the IECON*, vol. 1, pp. 354-359, 1993.

[7] L.K. Norford, and S.B. Leeb, "Non-intrusive electrical load monitoring in commercial buildings based on steady-state and transient load-detection algorithms," *Energ. Buildings*, vol. 24, pp. 51-64, 1996.

[8] U.A. Khan, S.B. Lee, and M.C. Lee, "A multiprocessor for transient event detection," *IEEE T. Power Deliver.*, vol. 12, pp. 51-60, 1997.

[9] H.H. Chang, C.L. Lin, and J.K. Lee, "Load Identification in Nonintrusive Load Monitoring Using Steady-State and Turn-on Transient Energy Algorithms," *Proc. of the 2010 14th Int. Conf. on Computer Supported Cooperative Work in Design*, pp. 27-32, 2010.

[10] A.I. Cole, and A. Albicki, "Nonintrusive identification of electrical loads in a three-phase environment based on harmonic content," *Proc. of the IEEE IMTC Conf.*, pp. 24–29, 2010.

[11] K.D. Lee, S.B. Leeb, L.K. Norford, P.R. Armstrong, J. Holloway, et al., "Estimation of variable-speed-drive power consumption from harmonic content," *IEEE T Energy Conver.*, vol. 20, pp. 566-574, 2005.

[12] D. Srinivasan, W.S. Ng, and A.C. Liew, "Neural-network-based signature recognition for harmonic source identification," *IEEE T. Power Deliver.*, vol. 21, pp. 398-405, 2006.

[13] C. Laughman, K. Lee, R. Cox, S. Shaw, S. Leeb, et al., "Power Signature Analysis," *IEEE Power Energy M.*, vol. 1, pp. 56-63, 2003.

[14] S.R. Shaw, S.B. Leeb, L.K. Norfold, and R.W. Cox, "Nonintrusive Load Monitoring and Diagnostics in Power Systems," *IEEE T. Instrum. Meas.*, vol. 57, pp. 1445-1454, 2008.

[15] W. Wichakool, A.T. Avestruz, R.W. Cox, and S.B. Leeb, "Modeling and Estimating Current Harmonics of Variable Electronic Loads," *IEEE T. Power Electr.*, vol. 24, pp. 2803-2811, 2009.

[16] A.S. Ardeleanu, C. Donciu, "Frequency estimation based on variable frequency resolution concept," *Proc. of the 2012 Int. Conf. and Exp. on Electrical and Pow. Eng.*, pp. 309-313, 2012.

[17] C. Donciu, C. Temneanu, and R. Ciobanu, "Breaking Nyquist criteria using alias frequencies interpretation," *Proc. of the 2005 IEEE Int. Conf. on Virtual Environments, Human Computer Interfaces and Measurement Systems,* 2005.

[18] C. Temneanu, C. Donciu, R. Ciobanu, and C. Schreiner, "Minimal fuzzy logic controller, design considerations and potential applications," *IEEE Int. Conf. on Computational Intelligence for Measurement Systems and Applications*, pp. 141-144, 2005.

[19] J. Liang, S.K.K. Ng, G. Kendall, and J.W.M. Cheng, "Load Signature Study—Part I: Basic Concept, Structure, and Methodology," *IEEE T. Power Deliver.*, vol. 25, pp. 551-560, 2010.

[20] J. Liang, S.K.K. Ng, G. Kendall, and J.W.M. Cheng, "Load Signature Study-Part II: Disaggregation, Framework, Simulation, and Applications," *IEEE T. Power Deliver.*, vol. 25, pp. 561-569, 2010.

[21] S.N. Patel, T. Robertson, J.A. Kientz, M.S. Reynolds, G.D. Abowd, "At the flick of a switch: detecting and classifying unique electrical events on the residential power line," *Proc. of the 9th Int. Conf. on Ubiquitous computing*, pp. 271-288, 2007.

[22] C. Donciu, and O. Costea, "Intelligent system for precision irrigation of greenhouse vegetables," *Proc. of 6th Int. Conf. on Manag. of Technol. Changes*, vol. 2, pp. 669-672, 2009.

[23] C. Donciu, O. Costea, M. Temneanu, R. Damian, and M. Branzila, "New prototype architecture for automated irrigation based on power line communication," *Grid Enable Remote Instrumentation*, pp. 499-509, 2009.

Modeling the GMI Effect in Amorphous Wires by Means of Electric Equivalent Circuits

Marinel Temneanu, Cristian Fosalau and Cristina Temneanu

"Gh. Asachi" Technical University, Iasi, Faculty of Electrical Engineering, Bd. D. Mangeron, 53, 700050, Iasi, Romania, phone +40232278680, Fax +40232237627, mtemnean@ee.tuiasi.ro

Abstract- An electric equivalent circuit for Co-based amorphous wires is studied in this paper. Its structure is based on some simple assumptions related to domain structure and the coupling between these domains but also on the presence of the specific relaxation mechanisms. Model parameters were identified using impedance spectroscopy techniques.

I. Introduction

Being one of the most promising magnetotransport phenomenons, the giant magnetoimpedance effect in amorphous wires and ribbons consist in a strong dependence of the sample impedance on an external magnetic field. A typical magnetic response of an AC voltage across a small sized Co-based sample is about 25%/Oe and 10%/Oe in the case of low frequency magneto-inductance and high frequency magnetoimpedance respectively [1]. This sensitivity explains the recent considerable interest for the applications in magnetic sensors [2], [3]. The electromagnetic origin of the MI effect has been attributed to the combination of the skin effect and the field dependence of the circumferential magnetic permeability associated with the circular motion of magnetic moments. Using impedance spectroscopy technique, this paper is investigating the influences of the external magnetic field on the parameters of a simple equivalent electric circuit proposed in [4].

II. Theoretical considerations

The equivalent circuit methodology consist in modelling the material's frequency response by means of an electric circuit with ideal passive components, usually associated with physical parameters of the material. An equivalent circuit founded to approximate with good accuracy the wire frequency behaviour has a series R_1 L_1 circuit connected to a parallel R_2 L_2 arrangement. R_1 accounts for the DC resistance, L_1 is related to the circumferential rotational permeability of the wire, L_2 and R_2 are associated with circumferential domain wall permeability and wall damping, respectively [4], [5]. For the proposed topology the expression of the complex impedance is:

$$Z^* = \left[R_1 + \frac{R_2 L_2^2}{R_2^2 + \omega^2 L_2^2}\omega^2\right] + j\omega\left[L_1 + \frac{R_2^2 L_2}{R_2^2 + \omega^2 L_2^2}\right] = R_s + j\omega L_s \tag{1}$$

Some approximations in low and high frequency have to be done in order to determine the values of the circuit elements. As we intend to evaluate the model behaviour for frequencies between 100 Hz and 300 kHz, and based on some previously reported results, the following equations can be used:

$$\begin{aligned} \omega = 100Hz &: Z^* = R_1 + j\omega(L_1 + L_2) \\ \omega = 300kHz &: Z^* = (R_1 + R_2) + j\omega L_1 \end{aligned} \tag{2}$$

The results obtained in model identification are further presented in this paper.

III. Experimental results

This paragraph is detailing both the experimental setup used to collect data and the results expressed in terms of models parameter variations over the analysed frequency spectrum for different DC currents and consequently, different values of axial magnetic field intensity.

A. Experimental setup

We used as-quenched amorphous wire of nominal composition $(Co_{94}Fe_6)_{72.5}B_{15}Si_{12.5}$, 125 μm diameter and 2,2 cm. length, prepared by the in-water-rotating technique. The sample was placed in a small PVC tube positioned inside a solenoidal coil , with the tube axis parallel to the axis of the solenoid. The

ensemble was mounted in a special sample holder with firm electrical contacts and impedance measurements were carried out by means of a system build with a Novocontrol analyser (Alpha type) controlled by a PC. All data were measured at room temperature with wire axis established at 90 degrees in respect with earth's field. The AC current through the amorphous wire was kept constant (10 mA) and the DC current flowing through the solenoid was varied in the range 0–1 A. For each of the DC current values complete spectroscopic measurements were done at frequencies from 100Hz to 300 kHz.
A schematic representation of the experimental setup is presented in Figure 1

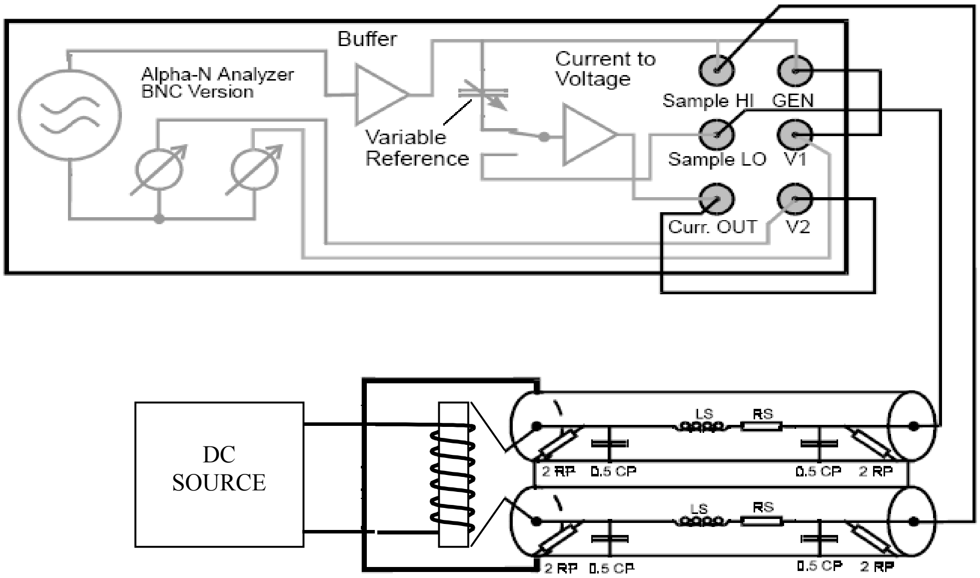

Figure 1. Schematic representation of the experimental setup

We used the recommended configuration [6] special attention being paid to the impedance compensation of the line from the analyser impedance inputs to the sample. The inductivities L_S and resistors R_S of the BNC lines contributing as a additional serial impedance to the measured one were taken into account using load short calibration and line compensation procedures. Because of the low value of the measured impedance, the R_P resistor has been considered large enough to be neglected. Also the capacitances C_P are requesting no compensation since they are eliminated by the virtual ground technique of the current input amplifier.

B. Results and discussions

Measured data were processed in order to emphasis the components of the complex impedance of the amorphous wire. Figure 2. shows the frequency dependencies of the equivalent serial inductance L_S and phase angle.

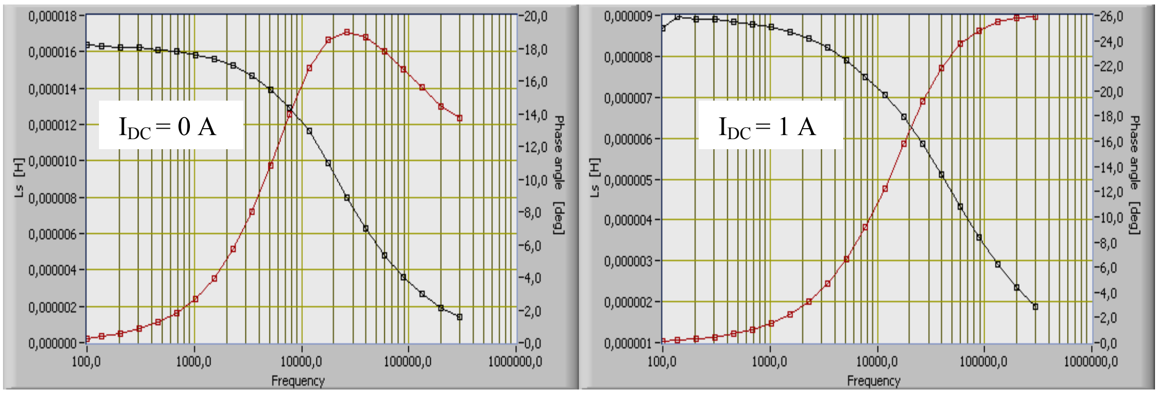

Figure 2. Frequency dependencies of the equivalent serial inductance and phase angle

It can be observed that the frequency behaviour show the features previously reported in other papers [4], [7], a relaxation domain being observed for both values of DC current flowing through the solenoidal coil. The equivalent serial inductance L_S usually associated with domain wall permeability decreases at high frequencies and the phase angle reveals a maximum at the relaxation frequency. A better illustration of the influences induced by the axial field over this specific behaviour is presented in Figure 3.

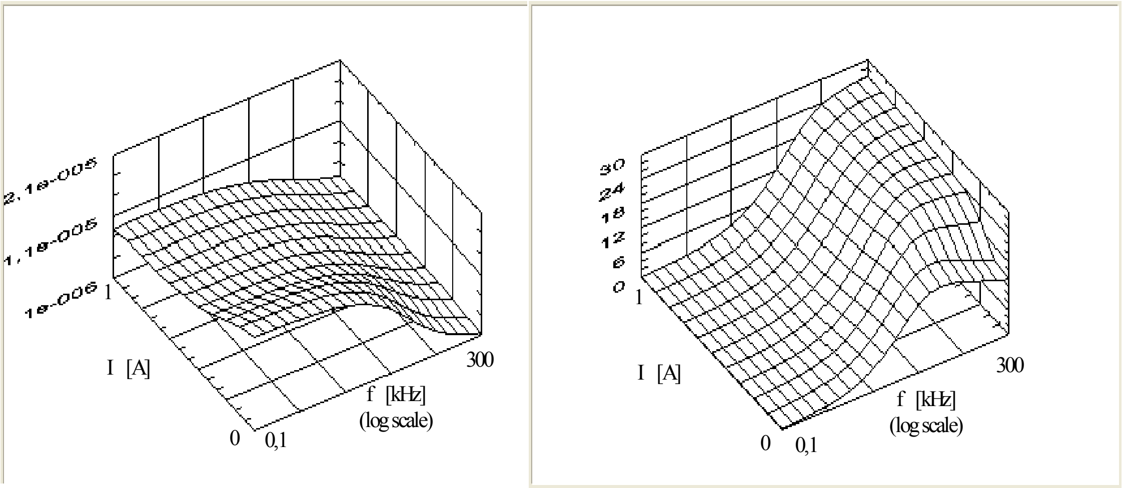

Figure 3. Equivalent serial inductance L_S and phase angle dependencies on frequency and DC current

There are represented the three dimensional surfaces of dependence for equivalent serial inductance and phase angle on frequency and I_{DC}.

Three important observations can be done:

- The general behaviour remains the same and therefore the axial field is to be considered only as an influence factor;
- For frequencies up to 20 kHz, where the skin effect is negligible, the serial inductance shows a decrease as the value of the DC current goes from 0 to 1A. This performance can be explained by the saturation effect occurring in high axial fields;
- The relaxation frequency is moving at higher frequencies (28 kHz for I_{DC}=0 and 300 kHz for I_{DC}=1A). This is essentially related to skin effects, the penetration depth being dependent on permeability which is lowered as the I_{DC} goes to 1A and we are approaching the saturation domain.

Basically there are two mechanism involved in this specific behaviour, the saturation effect and the skin effect. The shape of the characteristics is determined by their relative magnitude. In order to illustrate this, in Figure 4. are represented the dependencies of equivalent serial inductance L_S on I_{DC} for two frequency values, 100 Hz and 300 kHz. It is clear that once the skin effect is cancelled by the axial field (equally at high I_{DC}) the inductance is lowered by the increasing axial field, whatever frequency is considered. The saturation effect is stronger than the skin one. For low I_{DC} values and high frequency, the skin effect becomes important.

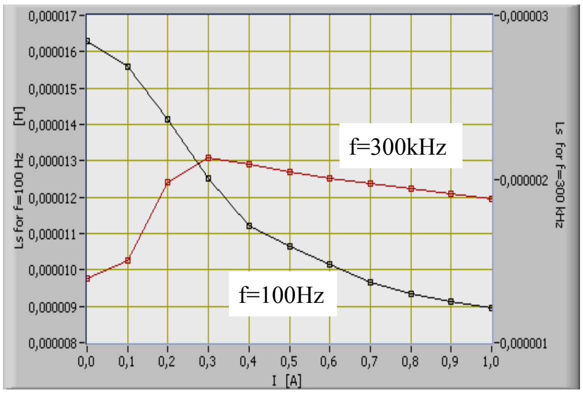

Figure 4. Equivalent serial inductance dependence on DC current flowing through the solenoid

Measured data have been processed according to (2) to identify the model parameters. The results are presented in Table 1.

Table 1. Model parameters for different DC current values

I [A]	0,000	0,100	0,200	0,300	0,400	0,500	0,600	0,700	0,800	0,900	1,000
L_1 [μH]	1,391	1,502	1,983	2,132	2,093	2,046	2,006	1,974	1,942	1,910	1,880
R_1 [Ω]	2,148	2,147	2,147	2,147	2,146	2,146	2,146	2,146	2,146	2,146	2,146
L_2 [μH]	14,91	14,08	12,17	10,39	9,135	8,600	8,136	7,672	7,387	7,228	7,085
R_2 [Ω]	8,567	8,579	8,026	6,990	6,482	6,148	5,853	5,623	5,436	5,295	5,152

The serial resistance R_1, computed from complex impedance's real part measured at 100Hz is in good accordance with previously reported results [4], [7]. It comprises not only the DC resistance of the amorphous wire but also the total contact resistance between the wire and the sample holder. As expected, low values were obtained for L_1, inductance associated with the rotational permeability of the wire. The parallel inductance L_2 is decreasing for large axial fields. Concurrently, the decreasing parallel resistance R_2 is confirming the strong coupling between the two mechanism discussed earlier in this paragraph.

IV. Conclusions

The magnetic behaviour of amorphous wires in terms of frequency dependence can be analysed using equivalent circuit methodology. Experimentally collected data reveal that the simple circuit topology proposed in [4] can be successfully used but model parameters must be adjusted in accordance with the relative magnitude between saturation and skin effects.

Acknowledgments This work has been supported by the Romanian Ministry of Education and Research under the MATNANTECH Project no. 258 (408) / 2004 in the frame of the PNCDI Program.

References

[1] L.V. Panina, K. Mohri, T. Uchiyama, M. Noda, K. Bushida, “Giant magneto-impedance in Co-rich amorphous wires and films” *IEEE Tran. On Magn*, vol.31, pp.1249-1260, 1995

[2] S. Sandacci, D. Makhnovskiy, L. Panina, K. Mohri, Y. Honkura, “Off-diagonal impedance in amorphous wires and its application to linear magnetic sensors”, *IEEE Tran. On Magn*, vol.40, pp.3505-3511, 2004

[3] K. Mohri, T. Uchiyama, L.P.Shen, C.M. Cai, L.V. Panina, Y. Honkura, M. Yamamoto, “Amorphous wire and CMOS IC-based sensitive micromagnetic sensors utilizing magnetoimpedance (MI) and stress-impedance (SI) effects” *IEEE Tran. On Magn*, vol.38, pp.3063-3068, 2002

[4] R. Valenzuela, M. Knobel, M. Vasquez, A. Hernano, “Effects of bias field and driving current on the equivalent circuit response of magnetoimpedance in amorphous wires”, *J. Appl. Phys.*, 28, pp. 2404–2410, 1995

[5] R. Valenzuela and I. Betancourt, “Giant Magnetoimpedance, Skin Depth and Domain Wall Dynamics”, *IEEE Tran. on Magn*, vol.38, pp.3081-3083, 2002

[6], *** “Alpha and Beta, Dielectric, Conductivity, Impedance and Gain Phase Analyzers - USER's Manual” *Novocontrol Technologies issue 1/2005*

[7] S. Song, S. Yu, K. Cheol and M. Vazquez, “Mechanism of Relaxation Dispersions of Permeability Spectra in Co-Based Amorphous Wire”, *IEEE Tran. On Magn*, vol.36, pp.3065-3067, 2000

12th IMEKO TC4 International Symposium
Electrical Measurements and Instrumentation
September 25–27, 2002, Zagreb, Croatia

IRON LOSSES MEASUREMENT USING SAMPLE AUTO-RANGING DATA ACQUISITION TECHNIQUES

Marinel Temneanu, Cristian Zet, Mihai Cretu, Cristian Fosalau

Faculty of Electrical Engineering, Technical University “Gh. Asachi” of Iasi, Romania

Abstract − Being one of the most important quality parameters of magnetic materials, iron losses, and consequently iron losses measurement, are extensively treated in scientific papers. There are many experimental set-up arrangements and also data processing algorithms proposed in order to improve the accuracy of measurement results. A sample auto-ranging data acquisition technique, implemented using National Instrument support, is presented in this paper. The experimental results obtained with three different A/D converters (12, 10 and 8 bits) are presented and compared with the results obtained by using the classic acquisition and processing algorithm.

Keywords: Iron losses, sample auto-ranging acquisition.

1. INTRODUCTION

The accurate measurement of the total amount of iron losses becomes more and more important since the magnetic materials used in our day’s equipments are subject to various magnetization regimes, both in frequency, amplitude and waveform of the magnetic induction. In low and medium intensity fields, with a sinusoidal waveform of induction, it seems that the well known integral method, which computes the iron losses from magnetizing currents and induced voltage, gives fairly good results. It is not the case of the high magnetic fields where the magnetizing current is strongly distorted. The reported relative errors are increasing once the saturation limit is exceeded. To better understand this, in Fig.1 is presented the typical experimental set-up used in magnetic measurements.

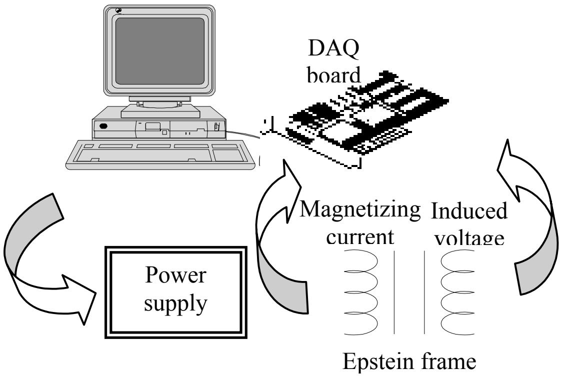

Fig.1 Information flow in magnetic measurement set-up

The material being tested is usually forming a closed magnetic circuit (toroidal or a squared). A programmable power supply, with current or voltage feedback, is used to prescribe the desired magnetizing regime. Using a shunt resistor and resistive voltage divider samples of the excitation current i(t) and induced voltage u(t) are acquired and digitally processed in order to determine magnetic quantities H(t) and B(t) with the well-known formulas:

$$\begin{cases} H(t) = \dfrac{N_1 i(t)}{l_m} \\ B(t) = B_0 - \dfrac{1}{N_2 A}\displaystyle\int_{to}^{t} u(t)dt \end{cases} \qquad (1)$$

where N_1, N_2, l_m, A and B_0 are the number of turns of the excitation and measurement windings, magnetic path length, cross section area and initial value ($t=t_0$) of magnetic field density respectively. If the excitation winding is supplied with an alternate symmetrical voltage the hysteresis loop is symmetrical too and the value of B_0 can be easily determined averaging the magnetic field density waveform over a period. The accuracy of the computed magnetic quantities is determined by the acquisition process of the electric ones. When experimental data are acquired using a DAQ system the analogic gain is usually determined by the peak value of the input signal. For all the samples the quantization error is less than 1/2 LSB. However, for those samples with small value, the relative error due to quantization is very high. With most of the commercially available systems, builded around a 12 bit A/D converter, this error can be neglected for a large number of signal waveforms. Unfortunately this is not the case in magnetic measurement. There are a lot of samples with small values in the waveform of the exciting current and, as we are approaching the saturation point, this number is increasing. Moreover these samples are multiply by the corresponding voltage values resulting in great relative errors in the iron losses evaluation. In order to reduce them, some authors have proposed a hardware method for sample self-scaling [1], [2]. On a classic data acquisition system, a sample and hold circuit before the programmable gain amplifier and a fast scaling device determine a 3 bit sample value which is used to modify the gain, is added. Other similar systems have been presented in literature [3], [4]. This paper makes use of a different approach, which requires no additional hardware, and it is easy to implement by software.

2. PROPOSED PROCEDURE

When acquiring a waveform with DAQ board, whatever programming utility is used (LabView, HPVEE, TestPoint, DAQ routines), the acquisition parameters cannot be modified "on the fly". We are referring here mostly at PGA's gain, sampling rate and number of samples. For example, once an acquisition is started in LabView, in order to reconfigure the input limits one should use again the AI Config.VI which means that the acquisition must first be stopped. The whole process being time consuming, only extremely low levels in sampling rate are addressing this technique (it depends on hardware support, but they are usually lower than 10 Hz). A different technique was proposed in order to replace the dynamic adjustment of the PGA's gain. Instead of changing the gain from one sample to another each signal is acquired with more than one gain (different channels) and then the original waveform is rebuild starting with the samples from the channel with highest gain. Each sample on this channel is first tested in order to verify if the channel is saturated (a maximum condition is imposed). If it is the case the second channel is taken into consideration and so on. For an extended presentation of the algorithm please refer to [5]

The method has some drawbacks the most important being:

- A smaller number of signals that can be acquired simultaneously (number of input channels on the DAQ board rated by number of gains used for each input signal);
- A lower sampling frequency (DAQ board maximum sampling frequency rated by number of gains used for each input signal).

If measurements have to be done in low frequency this algorithm is a very powerful tool in accurate evaluation. The purpose of our study is to determine the relative error made in iron losses measurements with two different data acquisition systems (8 bits and 10 bits A/D converters). The reference term is the result obtained by using a 12 bits A/D converter.

Experiments have been conducted using a standard (IEC 404-10) Epstein frame (grain oriented FeSi alloy), and three data acquisition boards with 12, 10 and 8 bits A/D converters respectively. An external signal was used to trigger the whole acquisition process.

For the data acquisition card equipped with an 8 bits A/D converter the following steps have been completed:

- The two input signals (magnetizing current and induced voltage) have been applied, each of them, to two input channels;
- Two different gains were programmed for these channels (1 and 2);
- Scaled data have been processed in order to avoid the phase shift due to the interchannel delay;
- The translated signals have been processed and the original signal rebuild.

In Fig. 2. are shown the results of these processes.

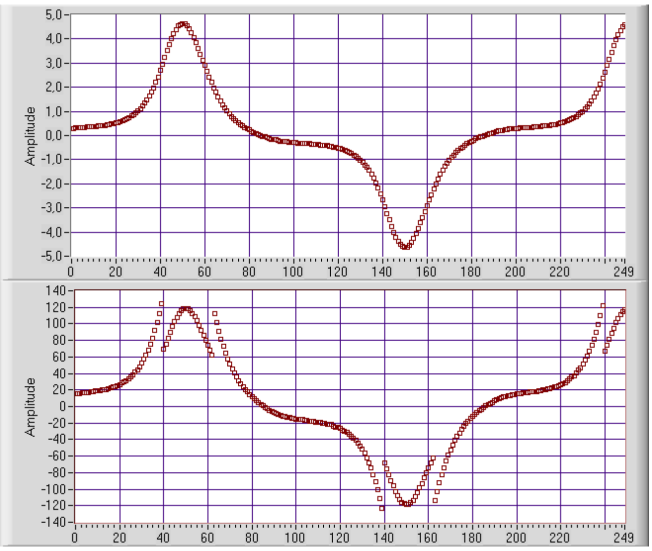

Fig.2 8 bits ADC. Data acquisition result (lower graph) and reconstructed waveform of magnetizing current (upper graph)

For the graphical presentation the acquired data have been decimated (1/4) in order to allow the observation of the differences between samples. Note that in the lower graph the sorted unscalled results are presented. It is clearly revealed that a large number of samples have been acquired with a gain value of 2 even if the peak value of the signal is approaching 5V (input limit of the channel). Only two gains (1 and 2) were used for each input signal because the board has 4 input channels.

For the DAQ board equipped with a 10 bits A/D converter three gains (1, 2 and 5) have been used for each input signal the same steps have been completed as for the previous presented board. The only differences consist in the number of channels used for each input signal and the number of programmed gains (three for each signal). The rest of the algorithm remains unchanged.

The results obtained are presented in Fig.3.

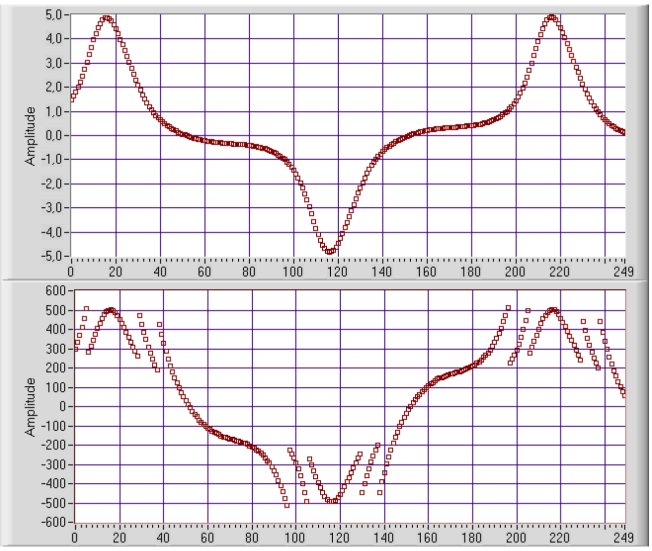

Fig.3 10 bits ADC. Data acquisition result (lower graph) and reconstructed waveform of magnetizing current (upper graph)

From the lower graph in Fig.3. (uncalled results) one may observe that most of the samples have been acquired with high resolution (channel with gain =5). Due to the specific shape of the magnetizing current waveform only few samples are selected from the second channel (gain=2) the rest of them being selected from the channel with gain=1.

In order to estimate the iron losses waveform of induced voltage was acquired, the results obtained with 10 bits ADC being presented in Fig. 4.

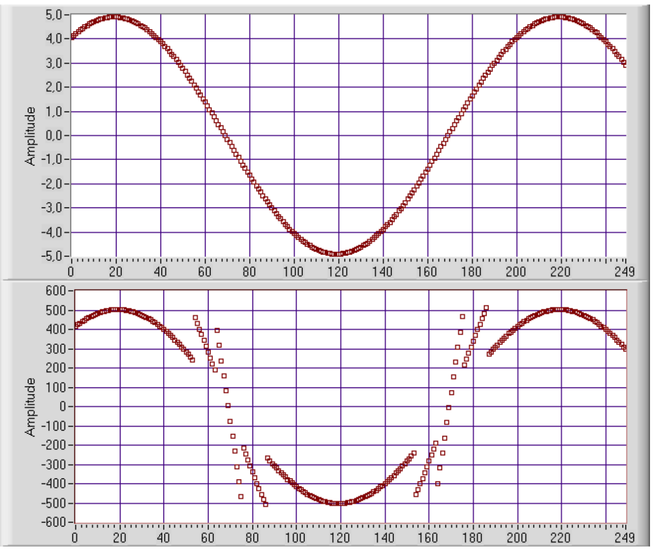

Fig.4 10 bits ADC. Data acquisition result (lower graph) and reconstructed waveform of induced voltage (upper graph)

It can be observed that, for the sinusoidally shaped induced voltage, only 24 samples from 250 have been acquired with high resolution.

3. EXPERIMENTAL RESULTS

In Fig.5 are represented the relative errors in iron losses estimation versus peak value of induced voltage. Two different curves are shown:

- the “one gain” 8 bits ADC relative errors curve;
- the “two gains” (1 and 2) 8 bits ADC relative errors one.

The values obtained by using the information provided by the 12 bits AD converter have been considered as the reference values.

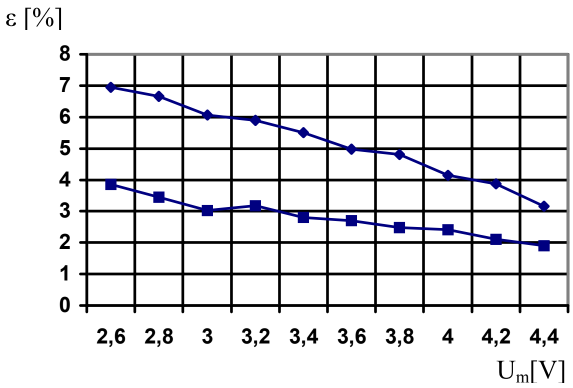

Fig.5 8 bits ADC. Relative errors in iron losses evaluation versus peak induced voltage. ♦ - 1 gain errors, ■ – 2 gain errors

As expected the relative error in iron losses measurement is decreasing when using a 2 gains acquisition techniques. A similar result, presented in Fig.6. was obtained for the 10 bits AD converter.

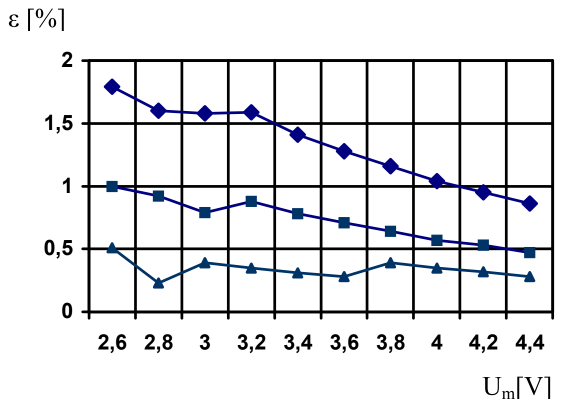

Fig.6 10 bits ADC. Relative errors in iron losses evaluation versus peakvalue of induced voltage.
♦ - 1 gain errors, ■ – 2 gain errors, ▲ – 3 gains

Three different curves are represented, relative errors versus peak value of induced voltage (adjusted to fit the DAQ input limits) for 1, 2 and 3 gains acquisition techniques (gain values – 1, 2 and 5). Once again the values obtained by using a 12 bits ADC have been considered as being the reference values.

4. CONCLUSIONS

It was emphasis in this paper that a more accurate evaluation of the iron losses can be done using a software sample auto scaling system. This technique is suited to analyze some intense magnetizing fields where classic data processing yields high relative errors.

5. FURTHER DEVELOPMENTS

As pointed before, one of the major drawbacks of the multi gain algorithm consists in the limitation of the number of input signals. Therefore it is necessary to develop some acquisition techniques allowing gain adjustments to be done “on the fly”. This can be done by changing the values of the PGA command lines between two scans. Only a low level registry-programming algorithm can be used in order to provide this facility. There are two possible solutions:

- to acquire one sample with gain=1, to evaluate the value and then to adjust the gain for the next reading;
- to compute the time derivative of the signal in each point, to predict the next value of the input and then to adjust the gain for the next sample.

The main advantage consists in the fact that there is no limitation on the number of gain used for each input signal.

ACKNOWLEDGMENT

This work was financed and developed in the framework of the LEONARDO DA VINCI pilot project with the contract number: RO/98/83550/PI

REFERENCES

[1] C. Zet, E. Vremera, "Hardware Method to Increase Speed and Accuracy in Multichannel Plug-In Data Acquisition Systems", *Proceedings of the 9th IMEKO-TC4 Symposium*, Glasgow, pp. 69-72, September, 1997.

[2] C. Zet, E. Vremera, "Improving Power Measurements Using Data Acquisition System with Hardware Self-Scaling", *Proceedings of the 10th IMEKO-TC4 Symposium*, Napoli, pp. 245-248, September, 1998.

[3] L.Grisoni, A. Heubi, P. Balsiger, F. Pelladini, "Implementation of a Micopower 15 bit Floating Point A/D Converter", *IEEE Transaction On Solid State Circuits*

[4] Francis Chen, C.S. Chen, "A High Speed High Resolution Floating Point Data Acquisition System", *IEEE Transaction on Industrial Application*, pp. 740-742, 1991

[5] Zet C., Temneanu M., Fosalau C., Cretu M., "Sample auto-ranging acquisition using National Instruments support" *IMEKO TC4 ADC Modelling and Testing Workshop*, Lisabona, pp. 177-150, 2001.

Authors:

Marinel Temneanu, Lecturer PhD, Electrical Measurement Dept., Faculty of Electrical Engineering, Bdul Mangeron, 53, Iasi, Romania, Phone: 4032278683/1240, Fax: 4032237627, E-mail: mtemnean@ee.tuiasi.ro

Cristian Zet, Lecturer PhD, Electrical Measurement Dept., Faculty of Electrical Engineering, Bdul Mangeron, 53, Iasi, Romania, Phone: 4032278683/1125, Fax: 4032237627, E-mail: czet@ee.tuiasi.ro

Mihai Cretu, Professor PhD, Electrical Measurements Dept., Faculty of Electrical Engineering, Bdul Mangeron, 53, Iasi, Romania, Phone: 4032278683/1122, Fax: 4032237627, E-mail: mcretu@ee.tuiasi.ro

Cristian Fosalau, Assoc. Professor PhD, Electrical Measurements Dept., Faculty of Electrical Engineering, Bdul Mangeron, 53, Iasi, Romania, Phone: 4032278683/1125, Fax: 4032237627, E-mail: cfosalau@ee.tuiasi.ro

12th IMEKO TC4 International Symposium
Electrical Measurements and Instrumentation
September 25–27, 2002, Zagreb, Croatia

FUZZY VERSUS NEURAL NETWORK MAGNETIC MODEL IN IRON LOSSES PREDICTION

Marinel Temneanu, Traian Balan, Dana Balan, Cristina Temneanu

Faculty of Electrical Engineering, Technical University "Gh. Asachi" of Iasi, Romania

Abstract – This paper emphasis the possibility to use both fuzzy and neural network based magnetic models in the prediction of the iron losses. The predictions are compared to the measured output for different magnetic materials and induction waveforms. Comparable results have been obtained proving the capacity of both techniques to describe the complex magnetic behavior of the materials being tested.

Keywords: Fuzzy, neural network, magnetic model.

1. INTRODUCTION

Magnetic materials, used in electric and electronic equipment, are subject to power losses, which may cause, in the case of bad material and/or design, failure in service. Being the interest of both industrial and academic research units, the prediction of iron losses has become the research subject of several multinational networks (see for example [1]). The involved phenomenon is very complex and therefore the practical approach is strongly dependent on the specificity of the magnetization regime. For a sinusoidal waveform of magnetic flux density the evaluation is usually done by using the specific loss data sheet provided by the material manufacturer, the only needed parameters being the frequency and the peak value of the induction in magnetic material. If the magnetization is a nonsinusoidal one the data sheet can still be used (knowing the frequency spectrum of induction) but the results are affected by large relative errors. In these cases two other techniques have been developed. The first one is addressing the iron losses with formulas describing each component (static, classic and excess loses) on the basis of time variation of magnetic induction [2]. The second one is assuming that a magnetic model can be identified from the experimental results and then the total losses can be calculated using their integral definition form. This last approach has recently result in many magnetic models some of them being included in computer aided design software used as a tool to predict the behavior of different electric equipments.

2. MODELS OF HYSTERESIS

Many mathematical approaches have been proposed in order to solve the problem of modeling the magnetic behavior of materials under simple or more complicated supply conditions. All of them are well defined for a specific geometric structure and there are reports on :

- simulation codes solving electromagnetic problems taking into consideration a direct monotonic continuous relationship between magnetic flux B and magnetic field H;
- models incorporating history dependent material properties [3],[4];
- models using spin up and down or using analytical functions, respectively [5];
- models implementing the concept of internal variables known from the field of irreversible thermodynamics and established in phenomenological modeling of inelastic mechanical behavior of solids [6].

Last decade can be characterized as the "upgrading decade" since most of the classic approaches have been combined with the Artificial Intelligence algorithms in order to result in more accurate magnetic models, [7]. Three of the AI components have been extensively used:

- artificial neural networks;
- fuzzy systems;
- genetic algorithms.

Artificial neural networks and fuzzy systems share a common objective: to emulate the operation of the human brain. In some sense, artificial neural networks try to emulate the hardware structure of the human brain – a massive connection of a huge number of simple neurons - while the fuzzy systems try to emulate our brain from a higher-level input-output point of view. Since most of the research conducted until today have been concentrated on implementing the AI techniques into the classic magnetic modeling framework, this paper is addressing two types of magnetic models (neural network and fuzzy system based) from a systemic point of view.

3. EXPERIMENT DESIGN

3.1. Input selection

As pointed before, the magnetic material is treated further on as a dynamic system and the objective is to find a suitable fuzzy model for its behavior. The first and probably the most important thing to do is to extract as much information as possible by using appropriate input signal. For linear systems a square input with random duty cycle gives maximal variance but for non-linear systems amplitude is also important and for this reason the experiments should involve as many amplitudes as possible. This signal must reveal all the important properties of the system being tested. In our case it must expose the saturation effect, the rate dependent hysteretic character and also the minor (second order) loops. Most authors [9] are suggesting the swept sinus with random frequencies as best candidate. In practice it is very difficult to obtain and control such signals so two other inputs (Fig.1) have been used (the same as in [8])

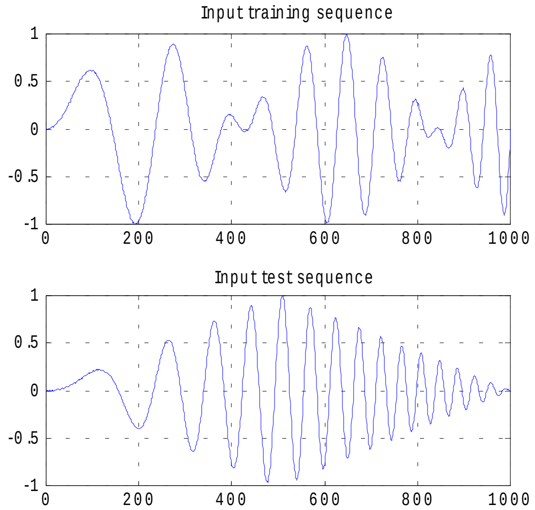

Fig.1 – Normalized value of magnetic field intensity (training and test sequences)

The central frequency value for the training sequence is 50 Hz and it is covering frequencies in the range 30-160 Hz (sine modulated). In order to test the identified fuzzy model a different shape was selected for the test sequence (central frequency – 50Hz, frequencies in 25-250 range, triangle modulation).

3.2. Choosing the structure and the regressors

The following structures are usually used in non-linear modeling:

- NFIR models – the vector of regressors is composed only on past inputs;
- NARX models – the vector of regresors has past inputs and past outputs;
- NOE models – the vector of regressors has past inputs and past estimated outputs;
- NARMAX models – as regressors past inputs , past outputs and estimation error are used.

A NARX assumption was used as describing the magnetic behavior and there are several reasons for this choice:

- It is easy to estimate due to the fact that its structure is non-recursive;
- The procedures that involve fuzzy clustering can only be applied on NARX models;
- We intend to compare the results with those reported in [8] where a neural network based NARX structure was used.

The predicted value of magnetic field density B_p is computed using *n* past outputs and *m* past inputs.

Choosing the right number of regressors is the next important step but, unfortunately, there are no easy and also secure methods to do this. For the case of fuzzy models Sugeno and Yasukawa suggest the use of the so-called regularity criterion (RC) combined with a search tree in order to find the inputs of the model but this search is not very efficient because the parameters of the model has to be calculated every time a candidate regressor is tested. Usually if the input signal has a signal to noise ratio greater than 10 dB another method [9] based on the evaluation of the Lipschitz quotients is used.

3.3. Fuzzy model identification and validation

Once the structure and the regressors being established another choice has to be done for the fuzzy model type - Mamdani or Takagi-Sugeno. The first one is a linguistic model describing a given system by means of linguistic if-then rules with fuzzy proposition in the antecedent as well as in the consequent. The Takagi–Sugeno (TS) fuzzy model on the other hand, uses crisp functions in the consequents. The choice is to be made based on the available sources of information for building fuzzy models: prior knowledge and/or data (process measurements). An important aspect here is the purpose of modeling. Following, the number, type and distribution of membership functions for each variable has to be established. This choice determines the level of granularity of the model. Again, the purpose of modeling and the detail of available knowledge, will influence this choice. Automated, data-driven methods can be used to add or remove membership functions from the model. After the structure is fixed, including here the inference mechanism, the operators and the defuzzification method, the performance of a fuzzy model can be fine-tuned by adjusting its parameters. Tunable parameters are the parameters of antecedent and consequent membership functions (determine their shape and position) and the rules. It ends with the model validation usually done by estimating the prediction error.

4. EXPERIMENTAL RESULTS

In order to obtain the relevant data a classic experimental set-up has been arranged. It contains a signal generator (Tektronix AFG310) followed by a power amplifier provided with a magnetizing current feedback. Two types of magnetic materials, grain oriented FeSi alloy and FeNi alloy have been tested in a standard 25 cm. Epstein frame (IEC 404-10). The data were collected with an AT-MIO 16E-10 DAQ board using a virtual magnetometer (LabView based) and processed in Matlab. As mentioned before, in order to compare the results with those obtained by neural network based modeling [8], a NARX predictor has been used, the vector of regressors being composed on two past outputs and one past input. Because of the large amount of data available, a Takagi-Sugeno fuzzy model was selected. Two software toolboxes, specially conceived for fuzzy modelling and identification have been used, Fuzzy Modeling and Identification Toolbox v303 [10] and Fuzzy Logic Toolbox v2 for Matlab developed by J-S Jang.

The first one build MIMO input-output static or dynamic fuzzy model from data by means of product-space clustering using the Gustafson-Kessel algorithm. The second one was used to build and identify neuro-fuzzy model with the so-called neuro-adaptive learning techniques incorporated into ANFIS in this toolbox.

The results obtained in modeling the behavior of grain oriented FeSi alloy are presented in Fig. 2. and Fig 3.

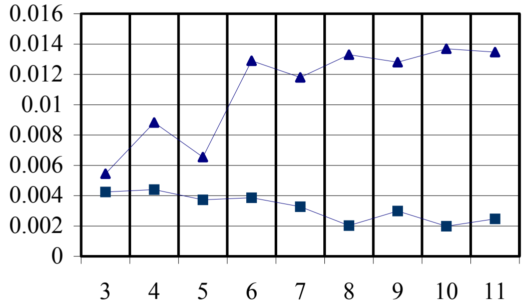

Fig. 2. Average prediction error on training sequence obtained with FMID (triangular markers) and ANFIS (squared markers)

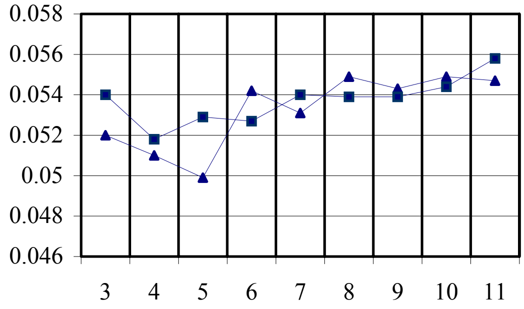

Fig. 3. Average prediction error on test sequence obtained with FMID (triangular markers) and ANFIS (squared markers)

It is remarkable that the average prediction error for both models remains at very low levels for the training and also for the test sequences. It can also be observed that the accuracy is maintained even if a small number of clusters (rules) are used. Moreover, a slightly improvement in prediction precision may be observed in these cases. For this reason further improvements have been tested only on the model that is using only 5 clusters with the structure depicted in Fig.4

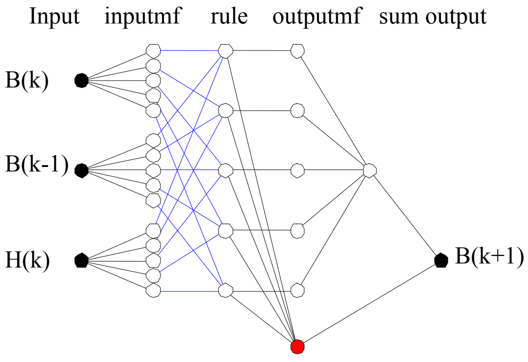

Fig. 4. Fuzzy model structure – 5 clusters before reduction

The rules obtained by tuning the parameters of the fuzzy model is presented in Table 1.

Table 1. Consequent parameters

rule	B(k)	B(k-1)	H(k)	offset
1	$2.05\cdot10^{0}$	$-1.16\cdot10^{0}$	$1.03\cdot10^{-1}$	$-2.48\cdot10^{-2}$
2	$2.00\cdot10^{0}$	$-1.03\cdot10^{0}$	$3.25\cdot10^{-2}$	$6.11\cdot10^{-4}$
3	$2.02\cdot10^{0}$	$-1.29\cdot10^{0}$	$4.43\cdot10^{-1}$	$2.22\cdot10^{-6}$
4	$2.02\cdot10^{0}$	$-1.22\cdot10^{0}$	$3.20\cdot10^{-1}$	$1.28\cdot10^{-3}$
5	$2.03\cdot10^{0}$	$-1.08\cdot10^{0}$	$3.83\cdot10^{-2}$	$1.15\cdot10^{-2}$

Every time when a model is identified it arise a new problem. Is this the best solution or it can be done more?

For the fuzzy models the next step is to simplify and reduce the model by merging by merging similar fuzzy sets and removing fuzzy sets similar to the universal one. Let’s take a look at the membership functions for the three inputs (Fig.5)

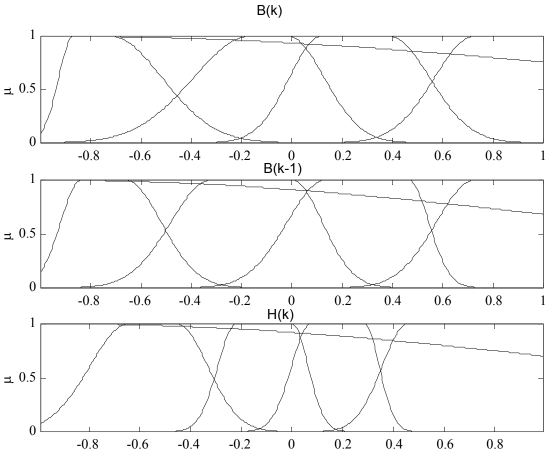

Fig. 5. Membership functions for the three inputs

The partition obtained by clustering the data look a little strange. There are no similar fuzzy sets but it is a set, in all three inputs memberships, which is very close to the universal one. There are powerful algorithms used for fuzzy model reduction but the results are not always acceptable. One of these, available in FMID Toolbox, was used for our model. The resulted structure is presented in Fig. 6 and the membership function for the remaining inputs in Fig. 7.

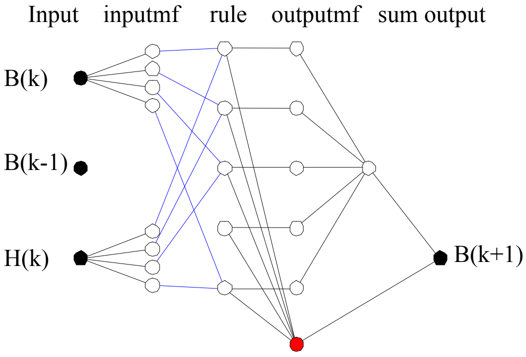

Fig. 6. Fuzzy model structure – 5 clusters after reduction

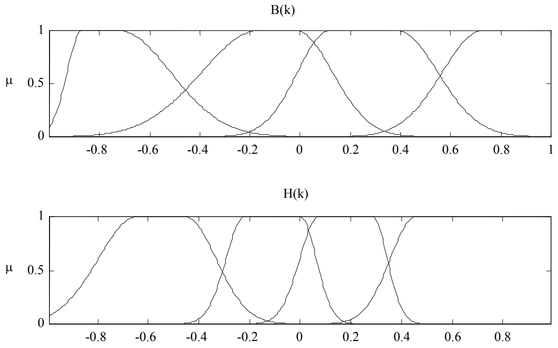

Fig. 5. Membership functions for the remaining two inputs

It is obvious that only 4 clusters remains and the partition look better, in terms of linguistic interpretation. Even the rules are simplified.

The surprise arrived from the fact that one input has been completely removed, only one past input and one past output being used to predict the next value of magnetic field density. The payoff for this simplicity is the lower accuracy of the model. For the test sequence the average prediction error is 0.12 for FMID (0.0497 before reduction) and 0.221 for ANFIS (0.053 before reduction). So the choice is to be made between linguistic relevance and modeling precision. The best fuzzy model, in terms of accuracy, was used for the prediction of the iron losses yielding the results presented in Table 2. There are also presented the result reported in [8] with neural network based models in order to be compared one with another.

Table 2 Iron losses evaluation using fuzzy magnetic model

	FeSi		FeNi	
	Max. relative error [%]	Conditions	Max. relative error [%]	Conditions
50 Hz	2,13	B_m=0,4 T	3,71	B_m=0,2 T
50 + 150 Hz	2,29	B_{m3}/B_m=0,15	4,33	B_{m3}/B_m=0,1
50 + 250 Hz	4,74	B_{m5}/B_m=0,1	4,86	B_{m5}/B_m=0,1

Table 3 Iron losses evaluation using neural network based magnetic model

	FeSi		FeNi	
	Max. relative error [%]	Conditions	Max. relative error [%]	Conditions
50 Hz	2,71	B_m=0,4 T	3,49	B_m=0,2 T
50 + 150 Hz	2,35	B_{m3}/B_m=0,15	5,10	B_{m3}/B_m=0,1
50 + 250 Hz	4,19	B_{m5}/B_m=0,1	4,23	B_{m5}/B_m=0,1

5. CONCLUSIONS

Different fuzzy models with lumped dynamic have been tested in order to give the prediction of the iron losses for a nonsinusoidal waveform of induction in FeSi (grain) and FeNi alloys. It was emphasis that using the same NARX assumption of the system, the same training and test input-output sequences and also the same number and structure of repressors, both fuzzy and neural network based magnetic models are yielding accurate evaluations. There are no significant differences between them and the choice is to be done only depending on user's ability to work with one or another.

ACKNOWLEDGMENT

This work was financed and developed in the framework of the LEONARDO DA VINCI pilot project with the contract number: RO/98/83550/PI.

REFERENCES

[1] EU Brite-Euram, "Characterisation of losses in electrical steels (CHARLES)", Project Rep. No. BRPR950019, 1998
[2] F. Fiorillo, A. Novikov, "Power losses under sinusoidal, trapezoidal and distorted induction waveform", *IEEE Trans. Magn*. vol. 26, pp. 2559-2561, 1990,
[3] F. Preisach, "Uber die Magnetishe Nachwirkung ", *Zeitschrift fur physic*, vol. 94, pp. 227-236, 1935
[4] I. Mayergoyz, "Mathematical models of hysteresis". *Springler*, New York, 1991.
[5] M. Saito, M. Namiki, S. Hayano, N. Tsuya, "Experimental verification of a Chua type magnetization model". *IEEE Trans. Magn.*, vol. 25, pp. 1876-1879, 1989.
[6] G.A. Maugin, M. Sabir, P. Chambon, "Coupled magneto mechanical hysteresis effects: application to nondestructive testing", in *Proc. of IUTAM*, pp. 255-258, 1987.
[7] A. Salvini, F.R. Fulginei, "Genetic algorithms and neural networks generalizing the Jiles-Atherton model of static hysteresis for dynamic loops", *IEEE Trans. Magn.*, vol. 38, pp. 873-876, 2002
[8] M. Temneanu, T. Balan, D. Balan, O. Postolache , "Iron losses prediction using neural network based magnetic model", *IMEKO TC4 Symposium*, Lisabona, pp.374-377, 2001
[9] J.J. Espinosa, J. Vandewalle, "Fuzzy modelling and identification, a guide for the user" SISCTA, Singapore, pp.279-286, 1997
[10] R. Babuska, "Fuzzy modelling and identification", *PhD Thesis*, Technical University of Delft, 1996.

Authors:

Marinel Temneanu, Lecturer PhD, Electrical Measurements Dept., Faculty of Electrical Engineering, Bdul Mangeron, 53, Iasi, Romania, Phone: 4032278683/1240, Fax: 4032237627, E-mail: mtemnean@ee.tuiasi.ro

Traian Balan, Professor PhD, Electrical Measurements Dept., Faculty of Electrical Engineering, Bdul Mangeron, 53, Iasi, Romania, Phone: 4032278683/1135, Fax: 4032237627, E-mail: tbalan@ee.tuiasi.ro

Dana Balan, Assoc. Professor PhD, Electrical Fundamentals Dept., Faculty of Electrical Engineering, Bdul Mangeron, 53, Iasi, Romania, Phone: 4032278683/1135, Fax: 4032237627, E-mail: dbalan@ee.tuiasi.ro

Cristina Temneanu, PhD Student, Electrical Fundamentals Dept., Faculty of Electrical Engineering, Bdul Mangeron, 53, Iasi, Romania, Phone: 4032278683/1241, Fax: 4032237627, E-mail: ctemneanu@yahoo.com